

## Quarterly Technical Report

## Solid State Research

2003:4

---

**Lincoln Laboratory**  
MASSACHUSETTS INSTITUTE OF TECHNOLOGY  
*LEXINGTON, MASSACHUSETTS*



---

Prepared for the Department of the Air Force under Contract F19628-00-C-0002.

Approved for public release; distribution is unlimited.

20040514 078

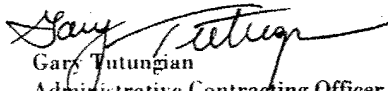
This report is based on studies performed at Lincoln Laboratory, a center for research operated by Massachusetts Institute of Technology. This work was sponsored by the Department of the Air Force under Contract F19628-00-C-0002.

This report may be reproduced to satisfy needs of U.S. Government agencies.

The ESC Public Affairs Office has reviewed this report, and it is releasable to the National Technical Information Service, where it will be available to the general public, including foreign nationals.

This technical report has been reviewed and is approved for publication.

FOR THE COMMANDER

  
Gary Tutungian  
Administrative Contracting Officer  
Plans and Programs Directorate  
Contracted Support Management

Non-Lincoln Recipients

PLEASE DO NOT RETURN

Permission is given to destroy this document  
when it is no longer needed.

**Massachusetts Institute of Technology  
Lincoln Laboratory**

**Solid State Research**

**Quarterly Technical Report  
2003:4**

**1 August – 31 October 2003**

**Issued 7 May 2004**

**Approved for public release; distribution is unlimited.**

**Lexington**

**Massachusetts**

## **ABSTRACT**

This report covers in detail the research work of the Solid State Division at Lincoln Laboratory for the period 1 August through 31 October 2003. The topics covered are Quantum Electronics, Electro-optical Materials and Devices, Submicrometer Technology, Biosensor and Molecular Technologies, Advanced Imaging Technology, Analog Device Technology, and Advanced Silicon Technology. Funding is provided by several DoD organizations—including the Air Force, Army, DARPA, MDA, Navy, NSA, and OSD—and also by the DOE, NASA, and NIST.

**THIS DOCUMENT CONTAINED  
BLANK PAGES THAT HAVE  
BEEN DELETED**

## TABLE OF CONTENTS

Abstract	iii
List of Illustrations	vii
List of Tables	xi
Introduction	xiii
Reports on Solid State Research	xv
Organization	xxiii
1. QUANTUM ELECTRONICS	
1.1 Energy-Scavenging Amplifiers for Miniature Solid State Lasers	1
2. ELECTRO-OPTICAL MATERIALS AND DEVICES	
2.1 Precision Calibration of an Optically Sampled Analog-to-Digital Converter	7
3. SUBMICROMETER TECHNOLOGY	
3.1 Ultraviolet Photolytic Derivatization for Sampling Low-Volatility Chemicals	11
4. BIOSENSOR AND MOLECULAR TECHNOLOGIES	
4.1 Assay Development Using CANARY	17
5. ADVANCED IMAGING TECHNOLOGY	
5.1 Intensity-Imaging Focal Plane Array Using Geiger-Mode Avalanche Photodiodes	23

6. ANALOG DEVICE TECHNOLOGY

6.1 Temperature Dependence of Intermodulation Distortion in YBCO	33
--	----

7. ADVANCED SILICON TECHNOLOGY

7.1 Elimination of Parasitic Channels in Fully Depleted SOI CMOS	37
--	----

## LIST OF ILLUSTRATIONS

Figure No.		Page
1-1	Energy-scavenging amplifier: (a) concept, (b) schematic of current embodiment, and (c) photograph of current embodiment.	2
1-2	Pulse energy and gain of energy-scavenging amplifier used with SPMCL-3. Different pump-diode temperature settings were used for data below and above 15 kHz. The pump diodes were operated in pulsed mode with 25-W peak power.	3
1-3	Amplifier gain as a function of pump duration. Data were taken at repetition rates between 500 Hz and 14 kHz, for a fixed pump-diode temperature. The line corresponds to Amplifier Gain = $1 + \text{Pump Duration} / 25 \mu\text{s}$ .	4
1-4	Pulse energy of energy-scavenging amplifier used with SPMCL-3 as a function of pump duration at several pulse rates. Pump duration is controlled by temperature tuning the pump diodes, as described in the text. Previous data refers to Figures 1-2 and 1-3.	5
2-1	Photonic analog-to-digital converter (ADC). $V(t)$ is the input signal to be digitized, and $V_A$ and $V_B$ are the digitized outputs from the photonic integrate-and-reset (PHIR) circuits.	7
2-2	Power spectrum of aliased 733-MHz sinusoid sampled using a 1-to-8 505-MS/s phase-encoded optical sampling ADC. The signal-to-noise and distortion is 61 dB (9.8 effective bits), and the input modulation index is 0.6.	9
3-1	Schematic diagram of integrated UV photolytic vaporization apparatus.	11
3-2	Ion mobility spectra of pure malathion after photolytic vaporization. The spectra on the left show raw spectra for (a) 172 nm in nitrogen, (c) 172 nm in air, and (e) 222 nm in air, whereas the spectra on the right are after the "lamp off" background spectra have been subtracted. Again, the spectra are for (b) 172 nm in nitrogen, (d) 172 nm in air, and (f) 222 nm in air. The annotations show the reduced mobility values.	13

## LIST OF ILLUSTRATIONS (Continued)

Figure No.		Page
3-3	Ultraviolet photolytic derivatization ion mobility spectroscopy (UPD-IMS) spectrum of 200 ng of malathion co-entrained with cotton lint particles irradiated with a 222-nm source, where (a) shows just the cotton lint, (b) the cotton lint with 200 ng of malathion added, and (c) the difference spectrum after subtraction of the spectrum for cotton lint. Peaks identified as 1 and 2 in (c) are attributable to malathion at $K_0$ values of 1.41 and 1.35 $\text{cm}^2 \text{V}^{-1} \text{s}^{-1}$ .	14
3-4	Normalized IMS signal as a function of the ratio of background aerosol to malathion. Slight signal enhancement is achieved when malathion is co-entrained with a dust, possibly because of increased scatter off dust particulates, allowing more malathion to be interrogated by the light source. The vertical bars labeled rural, urban, and sandstorm indicate typical ratio levels after collection of 200 ng of malathion at ambient concentrations of 0.01 $\text{mg}/\text{m}^3$ .	15
4-1	Results for (a) filter-and-replace and (b) centrifugal filtration methods for preparation of nasal swabs for detection of <i>B. anthracis</i> spores. In (a) a clear signal is seen with as little as 1000 spores, and in (b) as few as 50 cfu of <i>B. anthracis</i> spores are detected.	17
4-2	Results for urine prepared by filter-and-replace method after addition of (a) <i>C. trachomatis</i> and (b) <i>Y. pestis</i> . Because of the detection of as little as 200 cfu of <i>Y. pestis</i> in <5 min, this assay compares favorably with similar ones performed with nucleic acid tests, but is faster.	18
4-3	Detection of bacteria in human serum and whole blood with CANARY after (a) <i>Y. pestis</i> is added to 0.02 mL of serum, (b) <i>Y. pestis</i> is added to 0.1 mL of whole human blood, and (c) 50,000 cfu of <i>Y. pestis</i> is added to 6 mL of whole blood and processed according to M. Ewert's protocol. Although some loss of signal relative to the control (25,000 cfu) is still seen in (c), this result represents an improvement over (a) and (b).	20
4-4	(a) Detection of bacteria added to sputum before processing by the filter-and-replace method, and (b) results using M. Ewert's protocol, which reduces the effects of the interferant by at least tenfold and allows the detection of 100 cfu of <i>Y. pestis</i> added to the processed sputum.	21



## LIST OF ILLUSTRATIONS (Continued)

Figure No.		Page
5-1	(a) 10-Transistor pixel with 1-bit storage and active quenching, used on the T2 readout integrated circuit (ROIC), and (b) 11-transistor pixel with 1-bit storage and active quenching, used on the T3 ROIC.	23
5-2	(a) Fully functional $32 \times 32$ 50- $\mu\text{m}$ -pixel pitch T2 ROIC using scalable complementary metal-oxide semiconductor (CMOS) readout circuit architecture, and (b) T2 ROIC based focal plane array (FPA) with bump-bonded $16 \times 16$ array of 100- $\mu\text{m}$ -pixel pitch APDs.	24
5-3	(a) Test equipment for measuring integrated CMOS readout circuits and FPAs, and (b) T2 ROIC based FPA undergoing testing.	25
5-4	$16 \times 16$ Intensity images taken with two FPAs: (a) T2-Alpha, with 250-ns gate time, 1- $\mu\text{s}$ quench time, and $\sim 1500$ frames per second with 9-bit resolution, and (b) T2-Bravo, with 50-ns gate time, 50-ns quench time, and $>10,000$ frames per second with 9-bit resolution. The image in (b) shows the MATLAB graphical user interface window.	26
5-5	$16 \times 16$ Intensity images taken with T2-Bravo with (a) 250-ns gate time, 1- $\mu\text{s}$ quench time, and $\sim 1500$ frames per second with 9-bit resolution, (b) 250-ns gate time, 50-ns quench time, and $\sim 5100$ frames per second with 9-bit resolution, (c) 1- $\mu\text{s}$ gate time, 50-ns quench time, and $\sim 1900$ frames per second with 9-bit resolution, and (d) 10-ns gate time, 40-ns quench time, and $\sim 14,000$ frames per second with 9-bit resolution.	27
5-6	Avalanche photodiode (APD) dark count rate as a function of APD (a) overbias, (b) quench time, and (c) gate time.	28
5-7	$16 \times 16$ Intensity images taken with T2-Bravo with (a) 10-ns gate time and 20-ns quench time, and (b) 10-ns gate time and 10-ns quench time.	29
5-8	(a) Side view of all-stainless-steel front end of hermetically sealable cryogenic camera and (b) front view with hermetic window and imaging lens removed to reveal cooled FPA package and printed circuit board for support electronics.	30
5-9	Camera dewar: (a) front view, (b) side view showing refrigerant feedthroughs left beneath atmosphere control valve, and (c) back view showing atmosphere control valve, coolant, and electrical feeds.	31

## LIST OF ILLUSTRATIONS (Continued)

Figure No.		Page
6-1	Intermodulation distortion (IMD) vs circulating power for selected temperatures. This is for a pulsed-laser deposited film of $\text{YBa}_2\text{Cu}_3\text{O}_{7-\delta}$ . The dashed line illustrates slope 3, an indication of a $P_{\text{circ}}^3$ dependence.	33
6-2	Comparison of data and theory. The open circles are the IMD data, the solid line is the calculation of d-wave theory, and the dashed line shows $1/T^2$ behavior.	34
7-1	Schematic (top view) of (a) standard (edge) and (b) H-gate (edgeless) pMOS devices.	37
7-2	Subthreshold current-voltage (I-V) curves for standard pMOS, 21 devices each, across a 150-mm-diameter wafer.	38
7-3	Edge vs edgeless subthreshold I-V curves for standard pMOS, 21 devices each, across a 150-mm-diameter wafer.	38
7-4	Subthreshold I-V curves for standard pMOS with 6-keV B $p^+$ implant, 21 devices each, across a 150-mm-diameter wafer.	40
7-5	Subthreshold I-V curves for standard pMOS with 20-keV $\text{BF}_2$ $p^+$ implant, 21 devices each, across a 150-mm-diameter wafer.	40
7-6	Subthreshold I-V curves for standard pMOS with 2.5-keV B $p^+$ implant, 21 devices each, across a 150-mm-diameter wafer.	41
7-7	$I_{\text{on}}$ vs $I_{\text{off}}$ vs gate length for standard pMOS with 6-keV B $p^+$ implant. $V_d = -1.5$ V; $I_{\text{on}}$ at $V_g = -1.5$ V; $I_{\text{off}}$ at $V_g = 0.0$ V.	42
7-8	$I_{\text{on}}$ vs $I_{\text{off}}$ vs gate length for standard pMOS with 2.5-keV B $p^+$ implant. $V_d = -1.5$ V; $I_{\text{on}}$ at $V_g = -1.5$ V; $I_{\text{off}}$ at $V_g = 0.0$ V.	42
7-9	Plan view scanning electron micrograph of a standard 100/0.18- $\mu\text{m}$ device, showing the presence of a poly nodule.	43
7-10	Edge vs edgeless nMOS subthreshold I-V curves, without edge implant, 21 devices each, across a 150-mm-diameter wafer.	43
7-11	Edge vs edgeless nMOS subthreshold I-V curves, with edge implant, 21 devices each, across a 150-mm-diameter wafer.	44

## LIST OF TABLES

Table No.		Page
1-1	Characteristics of Several Microchip Laser/Energy-Scavenging Amplifier Combinations Operated at 500 Hz	6
7-1	Summary of Parameters Used to Identify the Cause of <i>p</i> MOS Shoulders	39

## INTRODUCTION

### 1. QUANTUM ELECTRONICS

The efficiency of longitudinally pumped miniature lasers has been enhanced by scavenging the unabsorbed pump light to pump an in-line amplifier. The system improvement is accomplished with minimal added cost, size, or complexity.

### 2. ELECTRO-OPTICAL MATERIALS AND DEVICES

An optically sampled analog-to-digital converter has shown promise as a means of achieving precision operation at high sampling rates. A procedure for calibration and post-correction of digitally converted samples yields a >72-dB spur-free dynamic range and >80-dB intermodulation suppression at a 505-MS/s sampling rate.

### 3. SUBMICROMETER TECHNOLOGY

An experimental apparatus to generate vapor signatures from malathion entrained in matrices of surface-impacted aerosols has been demonstrated using UV radiation from a barrier discharge lamp followed by detection via an ion mobility spectrometer. The application of this technique combined with a basic signal processing algorithm to decrease signal clutter shows promise as a viable field sensor concept for the detection of low volatility chemical aerosols.

### 4. BIOSENSOR AND MOLECULAR TECHNOLOGIES

Results have been obtained using CANARY (Cellular Analysis and Notification of Antigen Risks and Yields) to analyze several biological samples. Sensitivity with this method is comparable to that with immunoassay and polymerase chain reaction techniques, but in much less time.

### 5. ADVANCED IMAGING TECHNOLOGY

All-solid-state photon-counting focal plane arrays have been developed that comprise Geiger-mode avalanche photodiodes integrated with CMOS digital readout circuits. A compact camera system has also been developed that incorporates support electronics, imaging optics, and either thermoelectric or cryogenic cooling.

### 6. ANALOG DEVICE TECHNOLOGY

The third-order intermodulation distortion (IMD) vs power has been measured as a function of temperature from 1.7 K to  $T_c$  for a variety of YBCO films in a stripline resonator. The observed temperature and power dependence of the IMD are consistent with the nonlinear Meissner effect, which has been predicted for superconductors with d-wave symmetry.

## 7. ADVANCED SILICON TECHNOLOGY

Two different mechanisms that give rise to low-threshold parasitic channels and subthreshold shoulders in our fully depleted silicon-on-insulator process have been identified and eliminated. The process modifications have significantly improved subthreshold behavior of both  $n$ MOS and  $p$ MOS devices and have substantially improved performance and yield of complex circuits.

## REPORTS ON SOLID STATE RESEARCH

1 AUGUST THROUGH 31 OCTOBER 2003

### PUBLICATIONS

Nonlinear Surface Reactance of a Superconductive Strip	D. Agassi* D. E. Oates	<i>J. Supercond.</i> <b>16</b> , 905 (2003)
Measurement of the Auger Recombination Rate in <i>p</i> -Type 0.54 eV GaInAsSb by Time-Resolved Photoluminescence	S. Anikeev* D. Donetsky* G. Belenky* S. Luryi* C. A. Wang J. M. Borrego* G. Nichols*	<i>Appl. Phys. Lett.</i> <b>83</b> , 3317 (2003)
Magnetic Relaxation and Anisotropy Effects on High-Frequency Permeability	G. F. Dionne	<i>IEEE. Trans. Magn.</i> <b>39</b> , 3121 (2003)
Dense Only Phase Shift Template Lithography	M. Fritze B. Tyrrell R. Mallen B. Wheeler P. Rhyins* P. Martin*	<i>Proc. SPIE</i> <b>5042</b> , 15 (2003)
Nonlinear Microwave Response of Epitaxial YBaCuO Films of Varying Oxygen Content on MgO Substrates	M. A. Hein* R. G. Humphreys* P. J. Hirst* S. H. Park D. E. Oates	<i>J. Supercond.</i> <b>16</b> , 895 (2003)
Development of a UV LED Based Biosensor	T. H. Jeys L. Desmarais E. J. Lynch J. R. Ochoa	<i>Proc. SPIE</i> <b>5071</b> , 234 (2003)

---

\*Author not at Lincoln Laboratory.

Mass Transport: Semiconductor Microstructure Fabrication by Surface Energy	Z. L. Liao	<i>Mater. Sci. Eng. R</i> <b>42</b> , 41 (2003)
Marathon Evaluation of Optical Materials for 157-nm Lithography	V. Liberman M. Rothschild N. N. Efremow S. T. Palmacci J. H. C. Sedlacek A. Grenville K. Orvek	<i>J. Microlithogr., Microfab., Microsyst.</i> <b>2</b> , 19 (2003)
Progress in GaN-Based Materials and Optical Devices	I. D. Melngailis	<i>Proc. SPIE</i> <b>5123</b> , 231 (2003)
Monolithically Series Interconnected GaInAsSb/AlAsSb/GaSb Thermophotovoltaic Devices with an Internal Back Surface Reflector Formed by Wafer Bonding	C. A. Wang R. K. Huang D. A. Shiau M. K. Connors P. G. Murphy P. W. O'Brien A. C. Anderson D. M. DePoy* G. Nichols* M. N. Palmisiano*	<i>Appl. Phys. Lett.</i> <b>83</b> , 1286 (2003)

#### PRESENTATIONS<sup>†</sup>

Low-Polarization Dependent High-Efficiency WDM	E. Popov* J. Hoose* B. Frankel* C. Keast M. Fritze T. Y. Fan D. R. Yost S. Rabe	SPIE 48th Annual Meeting, San Diego, California, 3-8 August 2003
--	--	--

\*Author not at Lincoln Laboratory.

<sup>†</sup> Titles of presentations are listed for information only. No copies are available for distribution.

High-Fill-Factor, Burst-Frame-Rate  
Charge-Coupled Device

R. K. Reich  
D. M. O'Mara  
D. J. Young  
A. H. Loomis  
D. D. Rathman  
D. M. Craig  
S. A. Watson  
M. D. Ulibarri\*  
B. B. Kosicki

SPIE 48th Annual Meeting,  
San Diego, California,  
3-8 August 2003

Laser-Induced Breakdown  
Spectroscopy for the Detection  
and Classification of Biological  
Aerosols

J. D. Hybl

Laser-Induced Breakdown  
Spectroscopy Workshop,  
Johns Hopkins University,  
Baltimore, Maryland,  
6 August 2003;  
Biological Science and  
Technology Research Outlook  
Workshop,  
MIT Lincoln Laboratory,  
Lexington, Massachusetts,  
11-14 August 2003

Laser-Induced Breakdown  
Spectroscopy of Biological  
Aerosols

J. D. Hybl  
T. H. Jeys

UK Ministry of Defence,  
Porton Down, United Kingdom,  
11-13 August 2003

Active Optical Detection of  
Biological Agent Aerosols

T. H. Jeys

UK Ministry of Defence,  
Porton Down, United Kingdom,  
11-13 August 2003

Development of a UV-LED Based  
Biosensor

T. H. Jeys  
L. Desmarais  
E. J. Lynch  
J. R. Ochoa

UK Ministry of Defence,  
Porton Down, United Kingdom,  
11-13 August 2003

---

\*Author not at Lincoln Laboratory.



HTS Films for High-Power Microwave Applications	D. E. Oates	Air Force Office of Scientific Research Annual Program Review, Santa Barbara, California, 13 August 2003
121 nm Lithography and Immersion Lithography	M. Rothschild	Informal Seminar, Semiconductor Leading Edge Technologies (Selete), Yokohama, Japan, 21 August 2003
MBE Growth of Antimonide-Based Materials	G. Turner	30th International Symposium on Compound Semiconductors, San Diego, California, 25-27 August 2003
Modification of Optical Coatings under Long-Term Laser Irradiation	V. Liberman T. M. Bloomstein M. Rothschild S. T. Palmacci J. H. C. Sedlacek	4th International Symposium on 157 nm Lithography, Yokohama, Japan, 25-28 August 2003
Improved Pellicles for 157-nm Lithography—A Nanocomposite Approach	V. Liberman J. H. C. Sedlacek T. H. Fedynyshyn R. B. Goodman R. Sinta	4th International Symposium on 157 nm Lithography, Yokohama, Japan, 25-28 August 2003
Fluids for Immersion Lithography at 157 nm	M. Switkes R. R. Kunz R. F. Sinta J. Curtin M. Rothschild	4th International Symposium on 157 nm Lithography, Yokohama, Japan, 25-28 August 2003
High- $T_c$ Microwave Materials and Applications	D. E. Oates	Invited Seminar, Technical University of Ilmenau, Ilmenau, Germany, 10 September 2003

Optical Sampling for High-Speed,  
High-Resolution Analog-to-Digital  
Converters

P. W. Juodawlkis  
J. J. Hargreaves  
R. D. Younger  
R. C. Williamson  
J. C. Twichell  
G. E. Betts\*

International Topical Meeting  
on Microwave Photonics,  
Budapest, Hungary,  
10-12 September 2003

Temperature Dependence of  
Intermodulation Distortion in  
YBCO

D. E. Oates  
S.-H. Park  
D. Agassi\*

6th European Conference on  
Applied Superconductivity,  
Sorrento, Italy,  
14-18 September 2003;  
Seminar, Karlsruhe Research  
Center,  
Karlsruhe, Germany,  
22 September 2003

Effect of Ca-Doping on the  
Nonlinear Microwave Properties of  
YBCO Thin Films

D. Seron\*  
D. E. Oates  
J. Mannhart\*  
G. Hammerl\*  
M. A. Hein\*  
P. J. Hirst\*  
R. G. Humphreys\*

6th European Conference on  
Applied Superconductivity,  
Sorrento, Italy,  
14-18 September 2003;  
Seminar, Karlsruhe Research  
Center,  
Karlsruhe, Germany,  
22 September 2003

A Unified Model for Partial-  
Depletion and Full-Depletion  
SOI Circuit Designs: Using  
BSIMPD as a Foundation

P. Su\*  
S. K. H. Fung\*  
P. W. Wyatt  
H. Wan\*  
M. Chan\*  
A. M. Nikenejad\*  
C. Hu\*

IEEE Custom Integrated  
Circuits Conference,  
San Jose, California,  
21-24 September 2003

---

\*Author not at Lincoln Laboratory.

Nonlinear Microwave Properties of  
Superconducting YBaCuO and  
Dielectric MgO

M. A. Hein\*  
P. J. Hirst\*  
R. G. Humphreys\*  
S. H. Park  
D. Seron\*  
D. E. Oates

48th International Scientific  
Colloquium,  
Technical University of  
Ilmenau,  
Ilmenau, Germany,  
22-26 September 2003;  
European Microwave Week,  
Munich, Germany,  
6-10 October 2003

Elimination of Parasitic Channels in  
Fully Depleted SOI CMOS

C. K. Chen  
C-L. Chen  
C. L. Keast  
V. Suntharalingam  
P. W. Wyatt  
J. A. Burns  
D. R. Yost  
P. M. Gouker

29th Annual IEEE International  
SOI Conference,  
Newport Beach, California,  
30 September–2 October 2003

Active Optical Detection of  
Biological Agent Aerosols

T. H. Jeys

IEEE Lasers and Electro-Optics  
Society, Boston Chapter  
Meeting,  
Waltham, Massachusetts,  
9 October 2003

Overview of Superconductive  
Qubits

K. Berggren  
J. Sage  
W. Oliver

13th Biannual U.S. Workshop  
on Superconductive  
Electronics,  
Loon Mountain,  
New Hampshire,  
19-23 October 2003

Rapid Fabrication of  
Nb-Al/AIO<sub>x</sub>-Nb Josephson  
Junction Circuits

B. Cord  
K. Berggren  
V. Bolkhovsky  
E. Macedo  
W. Oliver  
J. Sage  
T. Weir

13th Biannual U.S. Workshop  
on Superconductive  
Electronics,  
Loon Mountain,  
New Hampshire,  
19-23 October 2003

---

\*Author not at Lincoln Laboratory.

Superconductive Approach to  
Type-II Quantum Computation

W. D. Oliver  
K. K. Berggren  
J. P. Sage  
R. L. Slattery  
T. J. Weir

13th Biannual U.S. Workshop  
on Superconductive  
Electronics,  
Loon Mountain,  
New Hampshire,  
19-23 October 2003

Laser-Induced Breakdown  
Spectroscopy as a Bioaerosol  
Trigger

J. D. Hybl  
S. R. Berry\*  
X. T. Le  
E. J. Lynch

30th Annual Meeting of the  
Federation of Analytical  
Chemistry and Spectroscopy  
Societies,  
Fort Lauderdale, Florida,  
19-23 October 2003

Microchip Lasers and Applications  
in Fieldable Instruments

J. J. Zayhowski  
J. D. Hybl

30th Annual Meeting of the  
Federation of Analytical  
Chemistry and Spectroscopy  
Societies,  
Fort Lauderdale, Florida,  
19-23 October 2003

Wavelength (Spectrally)-Combined  
Fiber Lasers for HEL's

T. Y. Fan

6th Annual Directed Energy  
Symposium,  
Albuquerque, New Mexico,  
20-24 October 2003

CCD Soft-X-Ray Detectors with  
Improved High- and Low-Energy  
Performance

B. E. Burke  
J. A. Gregory  
A. H. Loomis  
M. Lesser\*  
M. W. Bautz\*  
S. E. Kissel\*  
D. D. Rathman  
R. M. Osgood  
M. J. Cooper

Nuclear Science Symposium,  
Portland, Oregon,  
21-24 October 2003

---

\*Author not at Lincoln Laboratory.

Wavelength Beam Combining of  
Laser Arrays

S. J. Augst  
A. K. Goyal  
R. L. Aggarwal  
T. Y. Fan  
A. Sanchez

16th IEEE Lasers and Electro-  
Optics Society Annual Meeting,  
Tuscon, Arizona,  
26-30 October 2003

975-nm and 915-nm High  
Brightness Slab-Coupled  
Semiconductor Laser Arrays

R. K. Huang  
L. J. Missaggia  
J. P. Donnelly  
C. T. Harris  
J. Plant

16th IEEE Lasers and Electro-  
Optics Society Annual Meeting,  
Tuscon, Arizona,  
26-30 October 2003

Sub-Volt- $V_{\pi}$  InGaAsP Electro-  
refractive Modulators Using  
Symmetric, Uncoupled  
Quantum Wells

P. W. Juodawlkis  
F. J. O'Donnell  
R. J. Bailey  
J. J. Plant  
K. G. Ray  
D. C. Oakley  
A. Napoleone  
G. E. Betts\*

16th IEEE Lasers and Electro-  
Optics Society Annual Meeting,  
Tuscon, Arizona,  
26-30 October 2003

Arrays of 111-V Semiconductor  
Geiger-Mode Avalanche  
Photodiodes

A. McIntosh

16th IEEE Lasers and Electro-  
Optics Society Annual Meeting,  
Tuscon, Arizona,  
26-30 October 2003

High Power 1.5  $\mu\text{m}$  InGaAsP Slab-  
Coupled Optical Waveguide  
Amplifiers and Lasers

J. J. Plant  
P. W. Juodawlkis  
R. K. Huang  
L. J. Missaggia  
J. P. Donnelly

16th IEEE Lasers and Electro-  
Optics Society Annual Meeting,  
Tuscon, Arizona,  
26-30 October 2003

---

\*Author not at Lincoln Laboratory.

## ORGANIZATION

### SOLID STATE DIVISION

D. C. Shaver, Head  
R. W. Ralston, Associate Head  
N. L. DeMeo, Jr., Assistant  
Z. J. Lemnios, Senior Staff  
K. J. Challberg, Administrative Staff  
J. D. Pendergast, Administrative Staff  
L. K. Soule-Hinds, Administrative Staff

#### SUBMICROMETER TECHNOLOGY

M. Rothschild, Leader  
T. M. Lyszczarz, Assistant Leader  
T. H. Fedynyshyn, Senior Staff  
R. R. Kunz, Senior Staff

Astolfi, D. K.  
Bloomstein, T. M.  
Cann, S. G.  
Creel, C. R.  
Efremow, N. N., Jr.  
Geis, M. W.  
Goodman, R. B.  
Krohn, K. E.  
Leibowitz, F. L.

Lennon, D. M.  
Lieberman, V.  
Palmacci, S. T.  
Pottebaum, I. S.  
Sedlacek, J. H. C.  
Spector, S. J.  
Stallman, J. B.  
Switkes, M.  
Yoon, J. U.

#### QUANTUM ELECTRONICS

A. Sanchez-Rubio, Leader  
T. Y. Fan, Assistant Leader  
T. H. Jeys, Senior Staff  
J. J. Zayhowski, Senior Staff

Aggarwal, R. L.  
Augst, S. J.  
Chann, B.  
Daneu, J. L.  
Desmarais, L.  
DiNatale, W. F.  
Goyal, A. K.  
Herzog, W. D.

Hybl, J. D.  
Le, X. T.  
Lynch, E. J.  
O'Brien, P. W.  
Ochoa, J. R.  
Ranka, J. K.  
Ripin, D. J.

#### ELECTRO-OPTICAL MATERIALS AND DEVICES

J. C. Twichell, Leader  
G. W. Turner, Assistant Leader  
J. P. Donnelly, Senior Staff  
D. L. Spears, Senior Staff  
C. A. Wang, Senior Staff  
R. C. Williamson, Senior Staff

Bailey, R. J.  
Calawa, D. R.  
Calawa, S. D.  
Connors, M. K.  
Duerr, E. K.  
Goodhue, W. D.  
Groves, S. H.  
Hargreaves, J. J.  
Harman, T. C.  
Harris, C. T.

Huang, R. K.  
Juodawlkis, P. W.  
LaForge, B. E.  
Liau, Z. L.  
Mahan, J. M.  
Mahoney, L. J.  
Manfra, M. J.  
McIntosh, K. A.  
McNulty, D. D.  
Missaggia, L. J.

Molnar, R. J.  
Mull, D. E.  
Napoleone, A.  
Nitishin, P. M.  
Oakley, D. C.  
O'Donnell, F. J.  
Plant, J. J.  
Shiau, D. A.  
Verghese, S.  
Younger, R. D.

#### BIOSENSOR AND MOLECULAR TECHNOLOGIES

M. A. Hollis, Leader  
T. H. Rider, Senior Staff

Cabrera, C. R.	Petrovick, M. S.
Graves, C. A.	Riley, M. M.
Harper, J. D.	Schmidt, T. L.
Lacirignola, J. J.	Schwoebel, E. D.
Mathews, R. H.	Theriault, K. A.
Nargi, F. E.	Towle, T. A.
Parameswaran, L.	Zook, C. E.

#### ANALOG DEVICE TECHNOLOGY

M. A. Gouker, Leader  
L. M. Johnson, Assistant Leader  
A. C. Anderson, Senior Staff

Allen, M. S.	Oates, D. E.
Bolkhovskiy, V.	Oliver, W. D.
Fitch, G. L.	Sage, J. P.
Ieni, S.	Santiago, D. D.
Lyons, W. G.	Seaver, M. M.
Macedo, E. M., Jr.	Slattery, R. L.
Messier, A. V.	Straayer, M. Z.
Murphy, P. G.	Weir, T. J.

#### ADVANCED IMAGING TECHNOLOGY

B. B. Kosicki, Leader  
R. K. Reich, Assistant Leader  
B. E. Burke, Senior Staff

Aull, B. F.	Lind, T. A.
Ciampi, J. S.	Loomis, A. H.
Cooper, M. J.	McGonagle, W. H.
Craig, D. M.	O'Mara, D. M.
Daniels, P. J.	Osgood, R. M.
Doherty, C. L., Jr.	Percival, K. A.
Doherty, P. E.	Rathman, D. D.
Dolat, V. S.	Renzi, M. J.
Felton, B. J.	Rose, M. K.
Gregory, J. A.	Stern, A.
Johnson, K. F.	Stevenson, C. N.
Lambert, R. D.	Young, D. J.

#### ADVANCED SILICON TECHNOLOGY

C. L. Keast, Leader  
V. Suntharalingam, Assistant Leader  
P. W. Wyatt, Senior Staff

Austin, E. E.	Knecht, J. M.
Berger, R.	Muldavin, J. B.
Bozler, C. O.	Newcomb, K. L.
Brunelle, M. R.	Rabe, S.
Burns, J. A.	Soares, A. M.
Chen, C. K.	Travis, L.
Chen, C. L.	Tyrrell, B. M.
D'Onofrio, R. P.	Warner, K.
Fritze, M.	Wheeler, B. D.
Gouker, P. M.	Wlodarczak, T. J.
Healey, P. D.	Yost, D.-R.
Healey, R. E.	Young, G. R.
Hu, W.	

# 1. QUANTUM ELECTRONICS

## 1.1 ENERGY-SCAVENGING AMPLIFIERS FOR MINIATURE SOLID STATE LASERS

Passively *Q*-switched microchip lasers have many attractive features and have found numerous applications [1]–[3]. However, their relatively low efficiency is an impediment to their use on energy-starved platforms, including small unmanned earth or space vehicles. The inefficiency of these longitudinally pumped devices is due, in part, to inefficient absorption of the pump light, owing to the short length of the gain medium. This becomes more pronounced in lasers designed for very short pulse lengths [4]. By scavenging the unabsorbed pump light to pump an in-line amplifier, the efficiency of the system can be more than doubled, with minimal added cost, size, or complexity [5].

The concept of an energy-scavenging amplifier is shown in Figure 1-1. In its simplest embodiment, a single lens is used to focus both the output of a longitudinally pumped miniature laser and the pump light transmitted by it into the gain medium of the amplifier. Since the waists of the output and pump light are not in the same location in the laser, their images will be in different locations in the amplifier. However, with proper positioning of the lens, there can be excellent overlap of the laser output and the scavenged pump energy in the amplifier. For efficient operation the magnification of the lens should be chosen so that the laser light is near or above the saturation fluence in the amplifying medium. For high-power passively *Q*-switched microchip lasers, this condition is easily met.

The gain medium of the amplifier should have a large gain cross section at the output wavelength of the laser and strongly absorb the pump radiation transmitted by it. For the Nd:YAG lasers discussed here, Nd:YVO<sub>4</sub> satisfies both of these conditions.

Initial tests of the amplifier were performed with a short-pulse passively *Q*-switched microchip laser (SPMCL-3 [4]) comprising a 0.5-mm-thick undoped-YAG input endcap, a 1.5-mm-thick Nd:YAG gain medium, a 1-mm-thick Cr<sup>4+</sup>:YAG saturable absorber, and a 0.5-mm-thick undoped-YAG output endcap, diffusion bonded to each other in the order listed. The Nd:YAG was doped at 1.1 at.% Nd, the Cr<sup>4+</sup>:YAG had 6 cm<sup>-1</sup> absorption at 1064 nm, and the output coupler had 55% reflectivity at 1064 nm and was antireflecting (AR) around 808 nm. This laser design was optimized for use in a high-resolution three-dimensional imaging laser radar [6] and is currently being used (without the amplifier) in fielded systems. The amplifier was a 4.5-mm-thick piece of 1 at.% Nd:YVO<sub>4</sub> with both faces AR coated at 808 and 1064 nm. The lens imaging the output of the laser into the amplifier was a commercially available doublet comprising two 11-mm-focal-length lenses, AR coated at 808 nm. The transmission of the lens pair at 1064 nm was 91%. The lens was positioned to maximize the output power of the amplifier, with a magnification of ~1.3.

The pump light was delivered via a multimode fiber with a 200-μm core diameter and 0.22 numerical aperture. The output of the fiber was imaged into the microchip laser with the same type doublet used between the laser and the amplifier, adjusted for a magnification of ~0.5. The pump diodes were



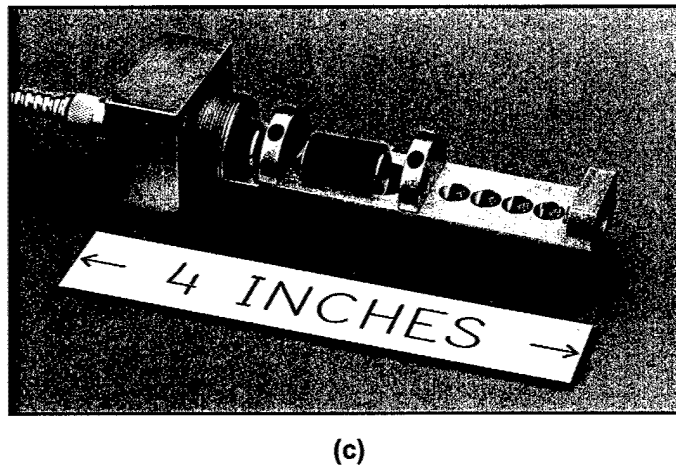
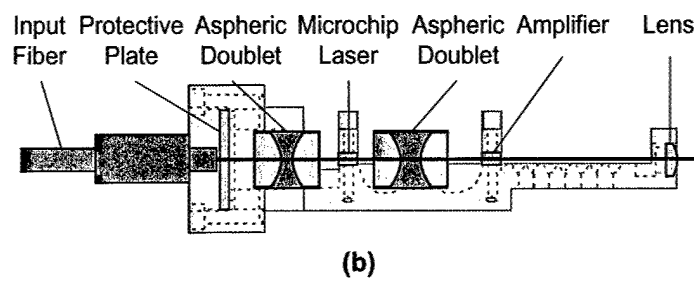
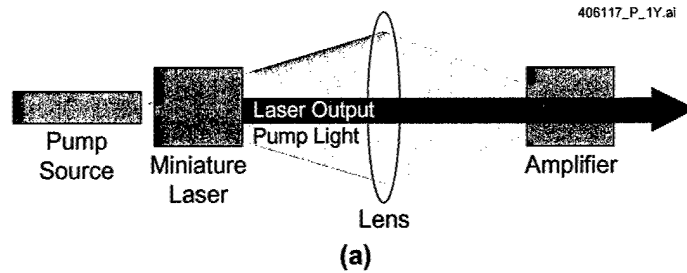


Figure 1-1. Energy-scavenging amplifier: (a) concept, (b) schematic of current embodiment, and (c) photograph of current embodiment.

operated in pulsed mode, turned on by an external clock and off by a signal generated when the microchip laser fired, with a peak power of 25 W. The temperature of the pump diodes was set at the same value for all data taken between 500 Hz and 14 kHz. Under these conditions the unsaturated transmission of the microchip laser was 44% for the pump light; the transmitted light was used to pump the amplifier. By readjusting the diode temperature, the data was extended to 17 kHz.

Without the amplifier the microchip laser produced  $\sim 27\text{-}\mu\text{J}$  pulses of  $\sim 370\text{-ps}$  duration. The output energy and gain of the amplifier are shown as a function of pulse repetition rate in Figure 1-2. Over the range tested the amplifier gain varied between 2 and 2.8, corresponding to a similar increase in system efficiency. In this experiment the pump duration changed as a function of pulse repetition rate. The gain of the system fit the equation  $\text{Amplifier Gain} = 1 + \text{Pump Duration}/25 \mu\text{s}$ , as shown in Figure 1-3. Since the inversion in the amplifier is nearly proportional to the pump duration, the amplifier efficiency was nearly independent of the inversion. This indicates that the laser light was focused tightly enough in the amplifier to exceed the saturation fluence and that the amplifier efficiency was limited by the overlap of the laser and pump light. The use of more heavily doped  $\text{Nd:YVO}_4$  would reduce the interaction length in the amplifier and allow better overlap and efficiency.

In the initial experiments the temperature of the pump diodes was adjusted to produce a near-minimum pump duration. By changing the temperature of the diodes, it was possible to detune their output from the  $\text{Nd:YAG}$  absorption peak, thereby decreasing the absorption of the microchip laser and

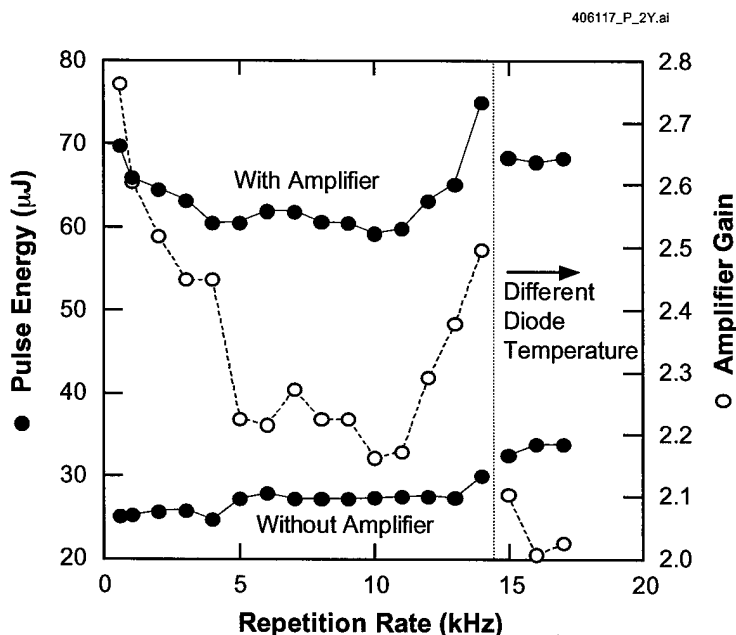


Figure 1-2. Pulse energy and gain of energy-scavenging amplifier used with SPMCL-3. Different pump-diode temperature settings were used for data below and above 15 kHz. The pump diodes were operated in pulsed mode with 25-W peak power.

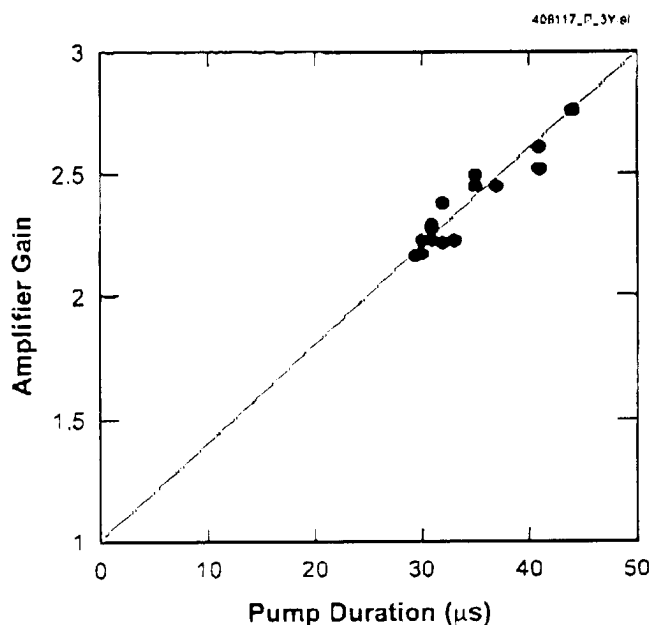


Figure 1-3. Amplifier gain as a function of pump duration. Data were taken at repetition rates between 500 Hz and 14 kHz, for a fixed pump-diode temperature. The line corresponds to Amplifier Gain =  $1 + \text{Pump Duration} / 25 \mu\text{s}$ .

increasing the pump duration required to reach threshold for a given peak pump power. The transmitted pump light was still efficiently absorbed by the Nd:YVO<sub>4</sub>, which has a broader absorption spectrum. The result is that the gain of the amplifier increases with the pump duration, as shown in Figure 1-4. The gain increase rolls off as the pump duration reaches the Nd:YVO<sub>4</sub> upper-state lifetime.

We next performed preliminary tests of the energy-scavenging amplifier with several other passively Q-switched microchip lasers. Each of the lasers selected represents a successful stand-alone design, optimized for a specific set of applications and used in fielded systems without the amplifier. The tests were performed at 500 Hz with the diode temperature adjusted to minimize the threshold of the laser (thereby minimizing the pump duration and the amplifier gain). The laser characteristics and test results are summarized in Table 1-1. The greatest efficiency enhancement, a factor of 2.8, was seen for the high-power, short-pulse microchip lasers, which have the greatest amount of transmitted pump light. The efficiency enhancement would be even higher using a properly polarized pump source (the pump light in the experiments reported here was unpolarized), since the absorption properties of Nd:YVO<sub>4</sub> are anisotropic. Even for the low-power microchip laser (LPMCL), pumped with an unpolarized source at a peak power of 2 W, the energy-scavenging amplifier yielded a 25% improvement in system efficiency.

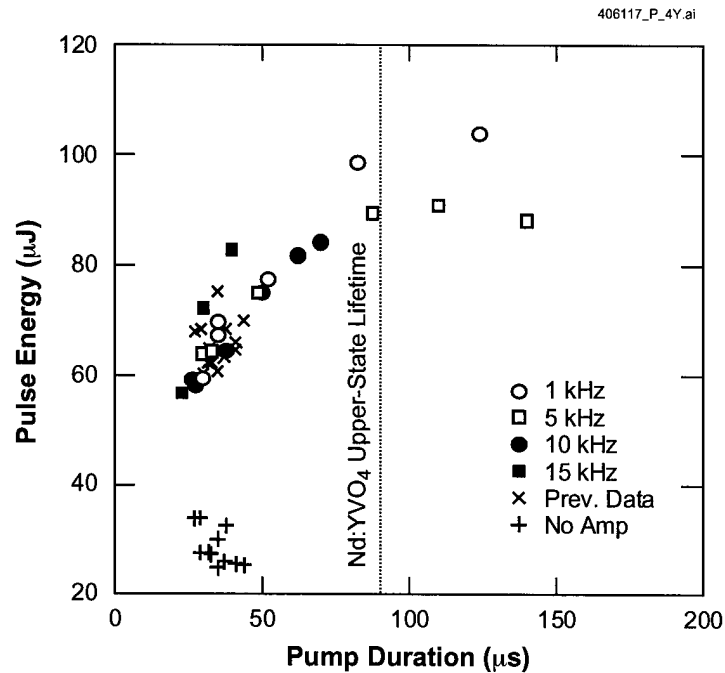


Figure 1-4. Pulse energy of energy-scavenging amplifier used with SPMCL-3 as a function of pump duration at several pulse rates. Pump duration is controlled by temperature tuning the pump diodes, as described in the text. Previous data refers to Figures 1-2 and 1-3.

Energy-scavenging amplifiers greatly enhance the efficiency of passively *Q*-switched microchip laser systems with minimal added cost, size, or complexity. The benefits of this approach undoubtedly extend to a much larger class of devices. When used with a high-power pump, the amplifier in a short-pulse microchip laser/energy-scavenging amplifier system is more efficient than the laser. Future designs for miniature lasers to be used with energy-scavenging amplifiers should take this into account. The results reported in this paper are preliminary, and were obtained with no effort to optimize the system. Things will only get better.

J. J. Zayhowski  
A. L. Wilson, Jr.

**TABLE 1-1**  
**Characteristics of Several Microchip Laser/Energy-Scavenging Amplifier**  
**Combinations Operated at 500 Hz**

Microchip Laser			Pump Characteristics		Microchip Laser Output		Amplifier Performance	
Laser	Cavity Design <sup>†</sup> $l_{ic}/l_{Nd}/l_{Cr}/l_{oc} - R$ (mm-%)	Unsaturated Pump Transmission (%)	Pump Duration ( $\mu s$ )	Pump Power (W)	Pulse Width (ps)	Pulse Energy ( $\mu J$ )	Output Pulse Energy ( $\mu J$ )	Gain
SPMCL-3	0.5/1.0/1.0/0.5 -55	44	44	25	370	25	70	2.8
SPMCL-6	—/1.0/1.0/— -55	44	70	15	250	21	59	2.8
SPMCL-0	1.0/3.0/1.5/1.0 -40	17	100	15	600	62	90	1.45
LPMCL	—/1.0/0.25/— -85	42	60	2	700	8.25	10.3	1.25
<sup>†</sup> $l_{ic}$ = length of input endcap, $l_{Nd}$ = length of gain medium, $l_{Cr}$ = length of saturable absorber, $l_{oc}$ = length of output endcap, and $R$ = reflectivity of output coupler at 1064 nm.								

### REFERENCES

1. J. J. Zayhowski and C. Dill III, *Opt. Lett.* **19**, 1427 (1994).
2. J. J. Zayhowski, *Laser Focus World* **35** (August), 129 (1999).
3. J. J. Zayhowski, *J. Alloys Compounds* **303–304**, 393 (2000).
4. J. J. Zayhowski and A. L. Wilson, Jr., *IEEE J. Quantum Electron.* **39**, 1588 (2003).
5. J. J. Zayhowski, U.S. Patent No. 6,512,630, 2003.
6. M. A. Albota, R. M. Heinrichs, D. G. Kocher, D. G. Fouché, B. E. Player, M. E. O'Brien, B. F. Aull, J. J. Zayhowski, J. Mooney, B. C. Willard, and R. R. Carlson, *Appl. Opt.* **41**, 7671 (2002).

## 2. ELECTRO-OPTICAL MATERIALS AND DEVICES

### 2.1 PRECISION CALIBRATION OF AN OPTICALLY SAMPLED ANALOG-TO-DIGITAL CONVERTER

Optically sampled analog-to-digital converters (ADCs) have shown promise as a means of achieving high-sampling-rate ADCs [1]–[3]. Attractive features include high input analog bandwidth in the optical modulators employed in sampling, low jitter in laser pulse trains, narrow optical pulses for sampling of high-frequency signals, and the use of optical demultiplexing to increase the effective overall rate of sampling and quantizing. While very high rate sampling has been demonstrated, most results have yielded signal-to-noise and spur suppression no better than about 48 dB or 8 bits. Many applications of ADCs, including radar, surveillance and some communication systems, require performance of more than 10 effective bits. Achieving this kind of precision in any high-speed ADC is a challenge.

The general configuration of the ADC that we have been developing is shown in Figure 2-1. A train of optical pulses samples the analog signal applied to the optical modulator. A dual-output Mach-Zehnder electro-optic modulator is used to implement phase-encoded optical sampling that yields both linearization and suppression of errors due to laser amplitude noise [2]–[4]. Output circuits detect and integrate the modulated optical pulses. The integrated level is held until the electronic digitizer converts the signal into digital form. After that, the circuit is reset and waits for the next input pulse. The output circuits include amplifiers before the digitizers.

For a system with an ideal modulator, linear detector, perfect photonic integrate-and-reset (PHIR) circuits, and wideband output amplifiers, the outputs  $V_A$  and  $V_B$  are given by  $V_A = E G_A [1 + \sin v(t)]$  and  $V_B = E G_B [1 + \sin v(t)]$ , where  $E$  is the energy in an optical pulse,  $G_A$  and  $G_B$  are overall gains to the two outputs, and  $v(t) = \pi V(t)/V_\pi$  is the normalized input voltage.  $V(t)$  is the voltage of the input analog signal at the time of sampling and  $V_\pi$  characterizes the modulator sensitivity. For this ideal situation, the only calibration needed is to equalize the gains  $G_A$  and  $G_B$ . In this case,  $v(t) = \sin^{-1}(PH)$ , where  $PH$  is a quantity we call the phasor given by  $PH = (V_A - V_B)/(V_A + V_B)$ .

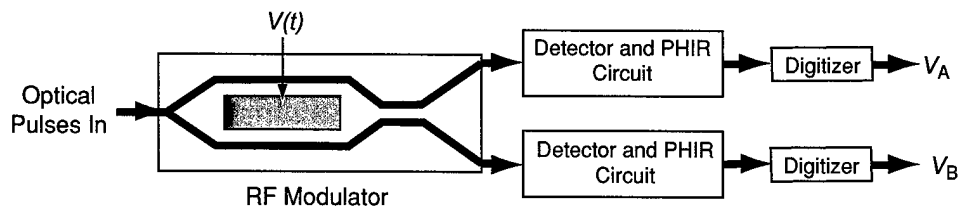


Figure 2-1. Photonic analog-to-digital converter (ADC).  $V(t)$  is the input signal to be digitized, and  $V_A$  and  $V_B$  are the digitized outputs from the photonic integrate-and-reset (PHIR) circuits.

However, a number of nonidealities, including differing finite contrasts  $C_A$  and  $C_B$  in the modulator, light-independent DC offsets  $V_{DCA}$  and  $V_{DCB}$ , and memory of the previous sample in the PHIR circuits, cause the actual situation to be much more complicated:

$$V_A = V_{DCA} + G_A E [1 + C_A \sin v(t)] + G_A E L_A [1 + C_A \sin v(t - \tau)] \quad (2.1a)$$

$$V_B = V_{DCB} + G_B E [1 + C_B \sin v(t)] + G_B E L_B [1 + C_B \sin v(t - \tau)] \quad (2.1b)$$

where  $\tau$  is one sample period,  $\tau = 1/f_s$  where  $f_s$  is the sampling frequency, and  $L_A$  and  $L_B$  are the fraction of the previous sample remaining in the PHIR outputs. In addition, with real detectors and output circuits,  $V_A$  and  $V_B$  are weakly nonlinear functions of the above expressions. If these corrupted values of  $V_A$  and  $V_B$  are used to calculate the phasor, significant nonlinear digitizing spurs result.

Hardware adjustments and device improvements were made to minimize  $L_A$  and  $L_B$  and to achieve high contrast ( $C_A \sim C_B \sim 1$ ). However, simulation and experiment showed that the corrupted phasor still yielded harmonics and spurs well above the 12-bit level. To yield better performance, digital post-correction of the samples can be applied. The first step is to turn off the laser and measure  $V_{DCA}$  and  $V_{DCB}$ . Previous-sample memory can be eliminated by subtracting off the proper fractions  $L_A$  and  $L_B$  of the previous sample. To determine this correction and the other needed corrections implied by Equation (2.1), a sinusoidal test tone with high modulation depth is injected into the modulator at a frequency close to  $f_s/4$ , where the distortions are most evident. A long data record is taken and Fourier transformed.  $L_A$  and  $L_B$  are adjusted in software until the phase of fundamental for the A output is exactly  $180^\circ$  relative to the phase of the B output as dictated by the complementary modulator outputs.

The parameters  $G_A$ ,  $G_B$ ,  $C_A$ , and  $C_B$  are difficult to measure directly. An indirect approach is used. When  $V_A$  and  $V_B$  are corrected for DC offsets and previous-sample memory, the resulting phasor is of the form  $PH = b + (1 + g) \sin v(t)$ , where both  $b$  and  $g$  are functions of the four parameters. A mathematical expansion yields

$$\sin^{-1}[b + (1 + g) \sin v(t)] = b + (1 + g)v(t) + bv^2(t) + gv^3(t) + \dots \quad (2.2)$$

Equation (2.2) implies that second harmonics of an input sinusoidal signal are due entirely to a finite value of  $b$  while third harmonics and intermodulation products are due entirely to a finite value of  $g$ . Appropriate corrections to  $PH$  are made by mathematically searching for a constant that when subtracted from  $PH$  suppresses the second harmonic in the Fourier transform of  $\sin^{-1}[PH^*]$ , where  $PH^*$  is the adjusted phasor. Similarly, a search is made for the gain adjustment of the phasor such that the third harmonic is suppressed. Modeling and experiment have shown that this process also corrects for nonlinearities in the detector and output circuitry and for errors in measuring  $V_{DCA}$  and  $V_{DCB}$ .

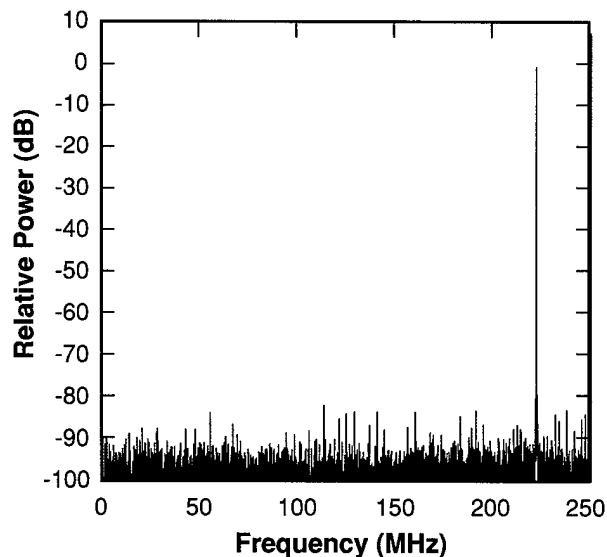


Figure 2-2. Power spectrum of aliased 733-MHz sinusoid sampled using a 1-to-8 505-MS/s phase-encoded optical sampling ADC. The signal-to-noise and distortion is 61 dB (9.8 effective bits), and the input modulation index is 0.6.

In order to increase the effective sampling rate of the optically sampled ADC, optical 1-to- $N$  demultiplexing of the output is utilized to yield an effective overall sampling that is  $N$  times faster than the maximum sampling rate of a single electronic digitizer. In our most recent system,  $N = 8$ . When the sequential samples are interleaved, interleaving spurs can result [5]. The initial step in calibrating the demultiplexed system is to perform the process described above for all eight channels in parallel. Then, the eight linearized outputs can be interleaved by simple offset and gain adjustments of the individual outputs such that the associated interleaving spurs are suppressed. Figure 2-2 demonstrates the performance achieved for a single-tone input whose frequency was chosen such that errors in the calibration process would be most evident. All spurs are suppressed to  $-82$  dB relative to the main signal. The signal-to-noise and distortion for an individual sample is 61 dB (9.8 effective bits). Similar tests at lower frequencies have yielded spur-free dynamic ranges over 72 dB. The results exceed the performance of any ADC in terms of combined sampling speed and effective number of bits. The calibration parameters drift over time, and work is under way to identify the system components that are varying, improve those components, and determine the minimum intervals between calibrations.

R. C. Williamson	R. D. Younger
P. W. Juodawlkis	J. J. Hargreaves
J. C. Twichell	



## REFERENCES

1. A. S. Bhushan, P. V. Kelkar, B. Jalali, O. Boyraz, and M. Islam, *IEEE Photon. Technol. Lett.* **14**, 684 (2002).
2. P. W. Juodawlkis, J. C. Twichell, G. E. Betts, J. J. Hargreaves, R. D. Younger, J. L. Wasserman, F. J. O'Donnell, K. G. Ray, and R. C. Williamson, *IEEE Trans. Microwave Theory Tech.* **49**, 1840 (2001).
3. T. R. Clark, Jr. and M. L. Dennis, *IEEE Photon. Technol. Lett.* **13**, 236 (2001).
4. J. C. Twichell and R. Helkey, *IEEE Photon. Technol. Lett.* **12**, 1237 (2000).
5. R. C. Williamson, P. W. Juodawlkis, J. L. Wasserman, G. E. Betts, and J. C. Twichell, *IEEE J. Lightwave Technol.* **19**, 230 (2000).

### 3. SUBMICROMETER TECHNOLOGY

#### 3.1 ULTRAVIOLET PHOTOLYTIC DERIVATIZATION FOR SAMPLING LOW-VOLATILITY CHEMICALS

The identification of harmful chemicals in the environment has been the focus of a wide number of field analytical studies. One class of chemicals receiving particular attention has been organophosphate pesticides, a class of neurotoxins harmful to humans, livestock, and wildlife. With the growing concern about an intentional, malicious release of such compounds as an act of terror, a means to quickly identify low-to-moderate concentrations of either vapors or aerosols using a small, inexpensive instrument would be desired.

The means to detect organophosphate vapors using small fieldable ion mobility spectrometer (IMS) instruments exists. (A number of suppliers produce chemical agent monitors based on ion mobility spectrometry, i.e., Smiths Detection and Draeger, which both produce and market such devices.) However, some compounds exhibit too low a vapor pressure for direct vapor phase measurement, and for these types of chemicals, they are more likely to be airborne as either homogeneous or heterogeneous aerosols.

Our investigations used the pesticide malathion as a model low-volatility organophosphorus neurotoxin. A method was developed to generate vapor signatures from organophosphate chemicals entrained within matrices of surface-impacted aerosol particles using UV radiation (172 or 222 nm) from a cw discharge lamp to photodissociate molecules collected within and on surface-impacted particles, as shown in Figure 3-1. Our work first involved using a gas chromatograph mass spectrometer to fully characterize the photochemistry of the primary products formed upon UV photolysis when vaporized in nitrogen ambient. Next, UV photolytic vaporization experiments were performed using an IMS to

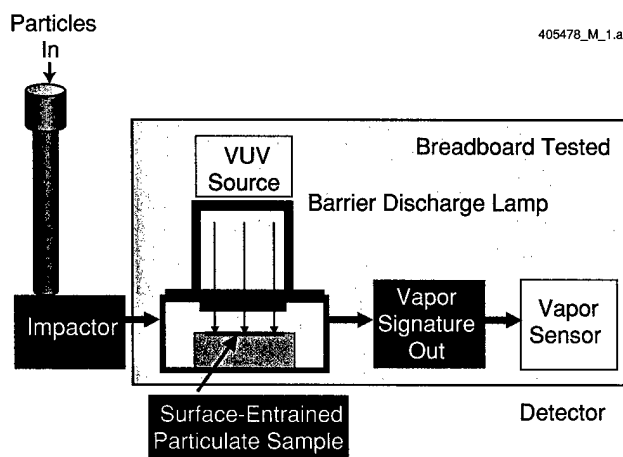


Figure 3-1. Schematic diagram of integrated UV photolytic vaporization apparatus.

determine the mobility spectra of the fragments from pure malathion generated under similar conditions. Finally, we investigated the ion mobility spectra for a variety of common background aerosols with and without trace amounts of malathion present. From these studies, conclusions can be drawn regarding the possibility for developing a field sensor based on this detection concept.

In IMS, the reduced mobilities,  $K_0$ , are the marker by which we identify the product peaks.  $K_0$  values that have been corrected to standard temperature and pressure were derived from the drift times and from measurement of the instrument's internal temperature and pressure. The instrument software uses the derived  $K_0$  values for spectral assignment, which can vary slightly. The relationship between drift time, temperature, and pressure is given by

$$K_0 = \left( \frac{d}{tE} \right) \cdot \left( \frac{273}{T} \right) \cdot \left( \frac{P}{760} \right) \quad (3.1)$$

where  $d$  is drift tube length (cm),  $t$  drift time (s),  $E$  electric field gradient ( $\text{V cm}^{-1}$ ),  $T$  temperature (K), and  $P$  pressure (Torr) [1].

Studies of malathion on a clean surface were conducted to determine the photolysis products under various experimental conditions. To isolate the spectra of the photolysis products from those resulting from instrument carryover, the spectra acquired prior to turning the lamp on were subtracted from those acquired while the lamp was on. The UV photolytic signature of malathion activated for the different experimental conditions tested is shown in Figure 3-2.

When detection of nonvolatile aerosols such as bacteria is performed via pyrolysis-IMS, the signal clutter due to background aerosols presents a major challenge. Interestingly, Arizona test dust, diesel fuel soot, diesel oil soot, bovine albumin, and *Bacillus globigii* all produced no detectable vapors using positive-mode IMS. However, cotton linters showed a complex signature with peaks with  $K_0 = 1.70, 1.61, 1.51, 1.45$ , and  $1.38 \text{ cm}^2 \text{ V}^{-1} \text{ s}^{-1}$ .

Despite the fact that most background aerosols tested showed no IMS signature, there was concern that they could obscure our ability to detect the target compound. In addition to signal clutter generated from co-vaporization from both malathion and background aerosols, the presence of background particulates can also have the physical effect of shadowing the UV radiation, thereby reducing the effective vaporization yield. For this reason, we also tested to see if malathion identification was still possible when co-entrained within a heterogeneous aerosol matrix. For these tests, an aerosol was impacted on a test surface, and 200 ng of malathion was drop cast directly on top of the dust. Initial mixed-matrix tests used cotton linters as the "background" material, and the surface was irradiated (222 nm lamp) both without and with malathion present, as shown in Figures 3-3(a) and 3-3(b), respectively. Subtraction of the dust sample from that which also contained malathion, i.e., Figure 3-3(b) minus Figure 3-3(a), such as would be performed as part of a target recognition algorithm in a real time sampler, reveals the presence of two peaks at  $K_0 = 1.41$  and  $1.35 \text{ cm}^2 \text{ V}^{-1} \text{ s}^{-1}$ , shown in Figure 3-3(c). This image closely resembles that for 200 ng of neat malathion where peaks at  $K_0 = 1.42$  and  $1.34 \text{ cm}^2 \text{ V}^{-1} \text{ s}^{-1}$  are observed, as shown in Figure 3-2(f).

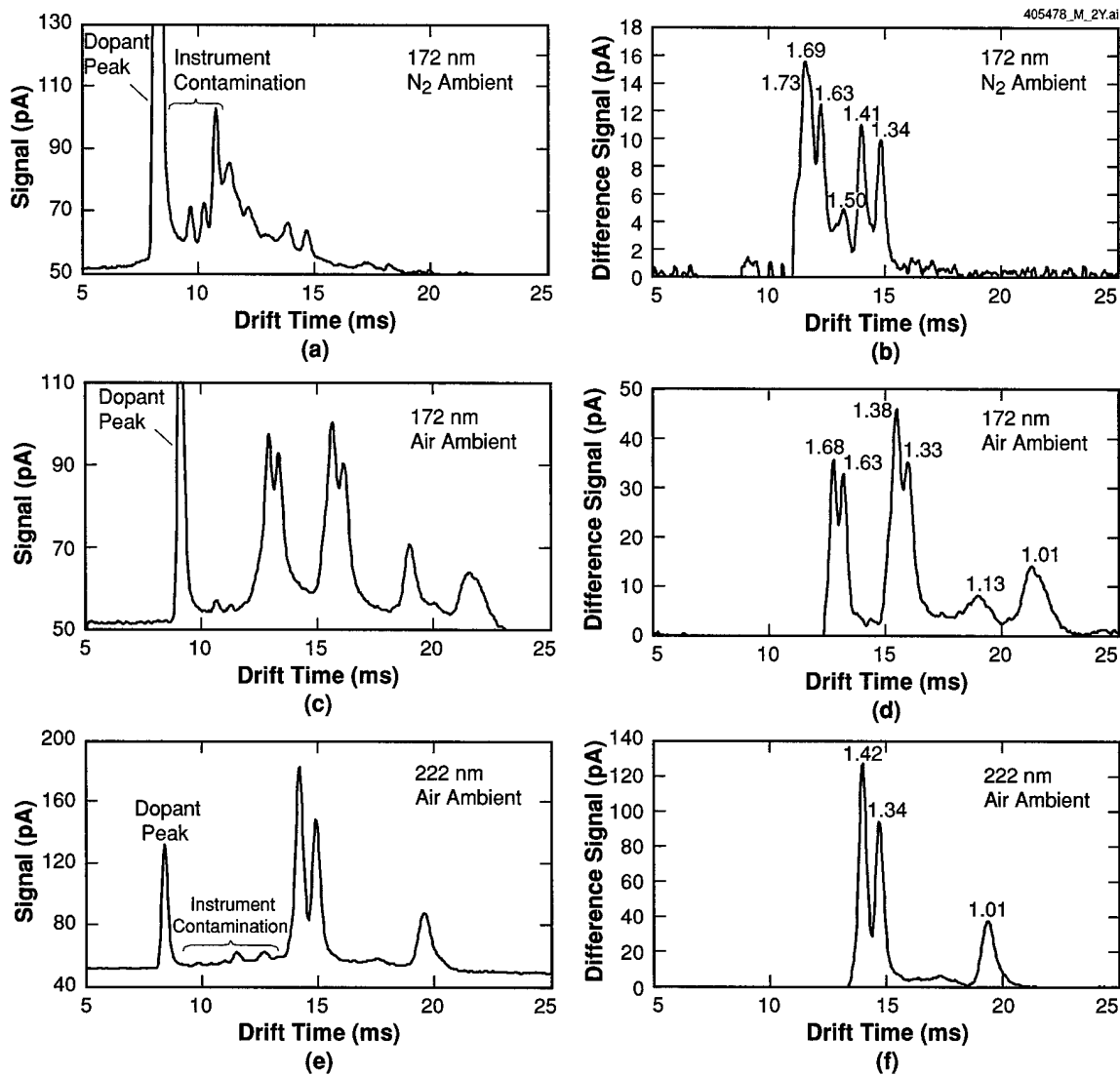


Figure 3-2. Ion mobility spectra of pure malathion after photolytic vaporization. The spectra on the left show raw spectra for (a) 172 nm in nitrogen, (c) 172 nm in air, and (e) 222 nm in air, whereas the spectra on the right are after the “lamp off” background spectra have been subtracted. Again, the spectra are for (b) 172 nm in nitrogen, (d) 172 nm in air, and (f) 222 nm in air. The annotations show the reduced mobility values.

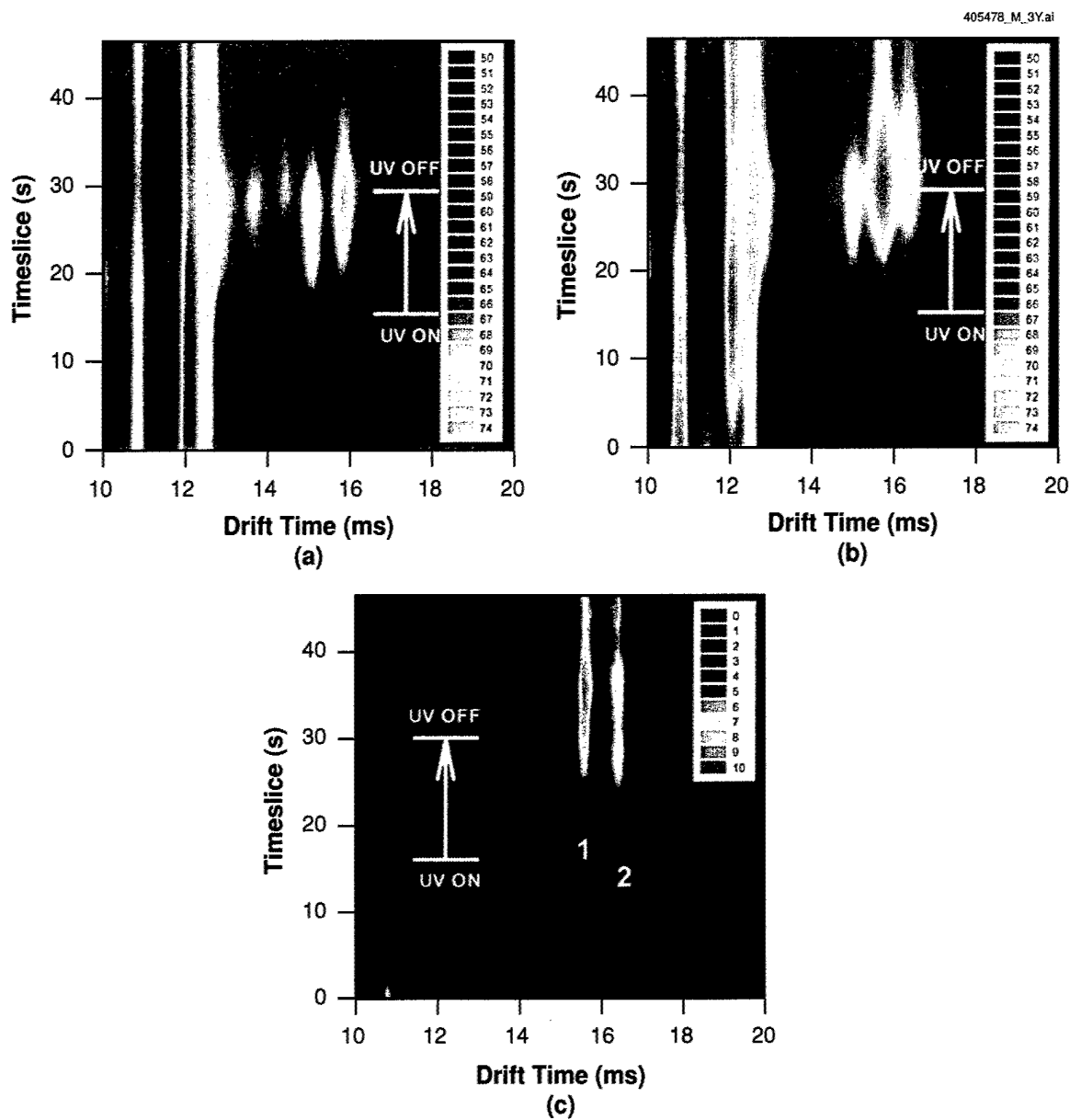


Figure 3-3. Ultraviolet photolytic derivatization ion mobility spectroscopy (UPD-IMS) spectrum of 200 ng of malathion co-entrained with cotton lint particles irradiated with a 222-nm source, where (a) shows just the cotton lint, (b) the cotton lint with 200 ng of malathion added, and (c) the difference spectrum after subtraction of the spectrum for cotton lint. Peaks identified as 1 and 2 in (c) are attributable to malathion at  $K_0$  values of 1.41 and 1.35  $\text{cm}^2 \text{V}^{-1} \text{s}^{-1}$ .

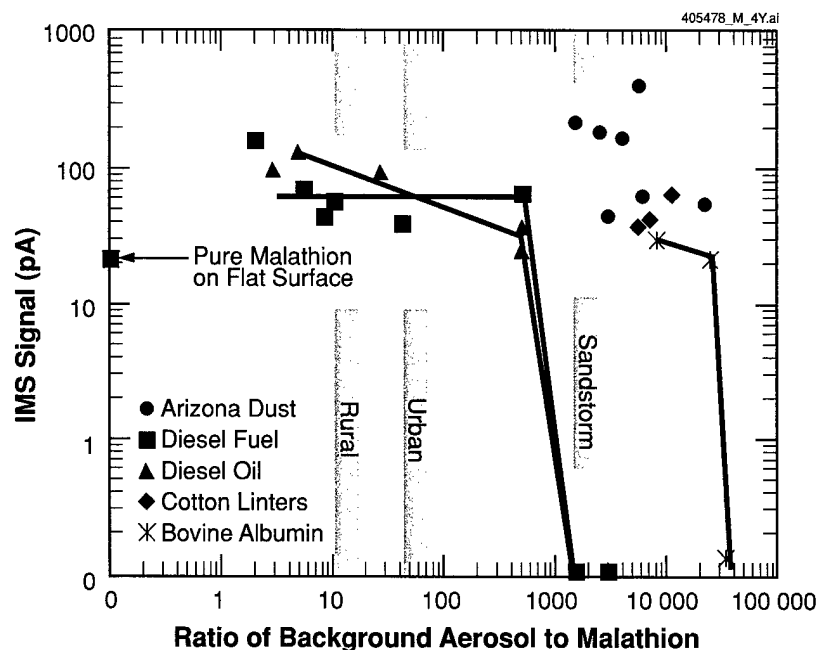


Figure 3-4. Normalized IMS signal as a function of the ratio of background aerosol to malathion. Slight signal enhancement is achieved when malathion is co-entrained with a dust, possibly because of increased scatter off dust particulates, allowing more malathion to be interrogated by the light source. The vertical bars labeled rural, urban, and sandstorm indicate typical ratio levels after collection of 200 ng of malathion at ambient concentrations of  $0.01 \text{ mg/m}^3$ .

Similar experiments were performed where 200 ng of malathion was added to increasingly larger amounts of simulated background aerosol consisting of Arizona test dust, diesel fuel soot, diesel oil soot, cotton linters, or bovine albumin. These results are shown in Figure 3-4, where we see significantly larger amounts (factors of  $10^3$  to  $10^5$ ) of background aerosol need to be present before the 200-ng malathion sample yields diminished signal. Interestingly, we see that the malathion signal actually *increased* in many cases as compared to the neat malathion on a clean surface. This behavior is attributed to both the increased surface area presented by the particulate ensemble and to UV light scattering, and to a lesser extent to refraction of the UV radiation thereby increasing the sample illumination efficiency. The background samples that are strong UV light absorbers, such as the soots, are going to pose a challenge to a UV photolytic technique as they both refract and scatter less radiation than other types of particulates. In contrast, the biggest signal enhancement was for the Arizona test dust. This we attribute to the relative transparency of the oxide particulates thereby allowing much more refraction of the incoming UV radiation within the particulate matrix and resulting in efficient sample illumination.

The results presented describe the phenomenology of UV photolytic vaporization of malathion. Quantities of malathion as small as 50 ng could be detected when the malathion was entrained on a clean

surface, and as small as 100 ng when co-entrained on a surface with much larger quantities of background aerosols. Given these results, estimates can be made for the detection limits of organophosphorus aerosols assuming that our observations for malathion are representative of this class of compounds. To make these estimates, we also assume that the instrument is coupled to a particle impactor in a manner analogous to the miniature matrix-assisted laser desorption ionization time-of-flight mass spectrometers under development to identify bioaerosols [2]. If a minimum of 100 ng of malathion is required on the photolysis surface to generate a measurable signal, and the particle impactor has an intake flow of 10 liters per minute, then the minimum detectable ambient concentration of malathion aerosol would be  $0.01 \text{ mg/m}^3$  for a 1-min sampling time. Typical background aerosols of respirable size can range from as low as  $<0.005 \text{ mg/m}^3$  in semi-arid areas to as high as  $>10 \text{ mg/m}^3$  in a sandstorm, with typical values being in the middle or low end of this range [3]. This would result in mass loading ratios of malathion to background material of as low as 1:1 to as high as 1000:1, all of which should have minimal impact on malathion detectability. These numbers compare favorably with sensitivities reported for vapor-based IMS devices, but the capabilities reported here would extend beyond vapors and provide an improved detection capability for nonvolatile aerosols.

R. R. Kunz  
F. L. Leibowitz  
D. K. Downs

#### REFERENCES

1. G. A. Eiceman, *Ion Mobility Spectrometry* (CRC Press, Boca Raton, FL, 1994).
2. C. W. Andersen and M. A. Carlson, *Johns Hopkins APL Tech. Dig.* **20**, 352 (1999).
3. R. Jaenicke, in *Aerosol-Cloud-Climate Interactions*, P. V. Hobbs, ed. (Academic, San Diego, 1993), pp. 1–31.

## 4. BIOSENSOR AND MOLECULAR TECHNOLOGIES

### 4.1 ASSAY DEVELOPMENT USING CANARY

Initial results obtained using CANARY (Cellular Analysis and Notification of Antigen Risks and Yields) [1] to analyze biological samples have been very promising compared to existing methods for analysis. Under clean laboratory conditions, immunoassay and polymerase chain reaction (PCR) techniques require at least 15–20 min to perform. However, sample preparation is often required with real samples, and as a result the time to perform these assays frequently increases to hours. Our results indicate that we can achieve sensitivity comparable to PCR in much less time.

A 5-min assay was developed for the detection of *Bacillus anthracis* spores on nasal swabs. Nasal passages were wiped with cotton swabs, which were subsequently seeded with formalin-inactivated *B. anthracis* Sterne strain spores. The swabs were rinsed in 1 ml of extraction medium, and the liquid was passed through a 5- $\mu$ m filter to remove large particulates. The eluate was centrifuged to concentrate the spores, and the liquid replaced with assay medium. The samples were then tested, and typical results are shown in Figure 4-1(a), where a clear signal is seen with as little as 1000 spores. Then, as seen in Figure 4-1(b), improvements to this method were achieved with the use of a centrifugal filtration device. In this

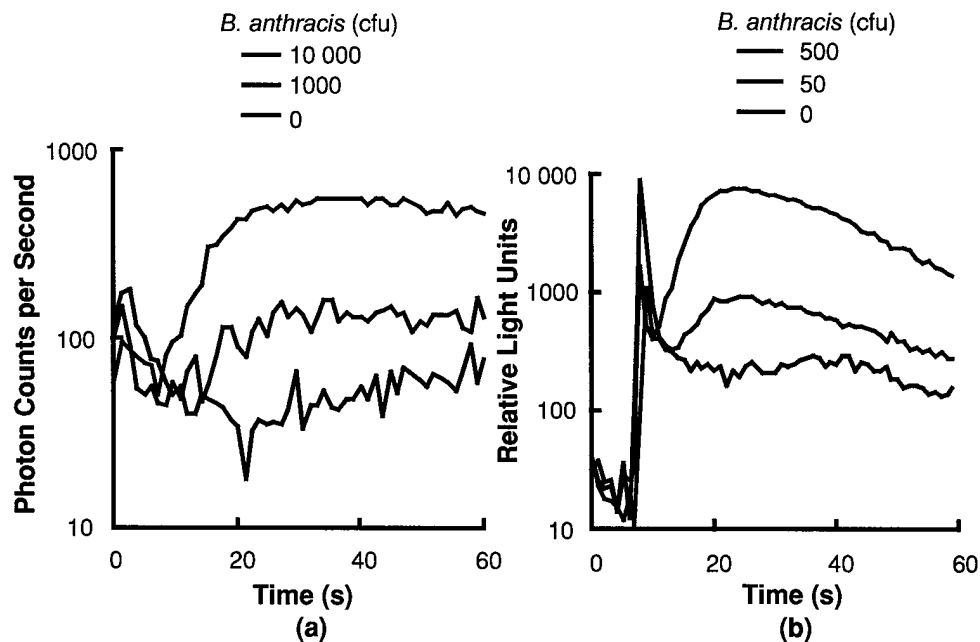


Figure 4-1. Results for (a) filter-and-replace and (b) centrifugal filtration methods for preparation of nasal swabs for detection of *B. anthracis* spores. In (a) a clear signal is seen with as little as 1000 spores, and in (b) as few as 50 cfu of *B. anthracis* spores are detected.



protocol the swabs were placed in a basket containing a 5- $\mu$ m filter with 400  $\mu$ L of assay medium. The eluate was collected in a 1.5-mL microfuge tube with a 2-min centrifugation, a step that also serves to concentrate the spores to the bottom of the tube. After centrifugation, the basket and swab were removed and the assay performed in the same tube. Not only does this protocol eliminate the transfer of the eluate to a syringe filter, it significantly improves recovery of spores from the swab, allowing the detection of only 50 spores added to the swab before elution.

A similar filter-and-replace protocol can be applied to the detection of bacteria in urine. Urine was seeded with bacteria and passed through a 5-mm syringe filter, the eluate was centrifuged for 2 min, and the liquid replaced with assay medium. Because of the rapid performance of CANARY, we were able to demonstrate detection of *Chlamydia trachomatis* in urine in <5 min, as shown in Figure 4-2(a). Since an enumerated preparation of *C. trachomatis* was not available, we performed the same experiment with bacteria for which we had a precise enumeration. In this experiment, we were able to detect 200 cfu of *Y. pestis* added to urine prior to sample preparation, as seen in Figure 4-2(b). This implies that CANARY would be useful as a rapid, sensitive test for the diagnosis of *C. trachomatis* infections using clinical samples acquired in a noninvasive manner.

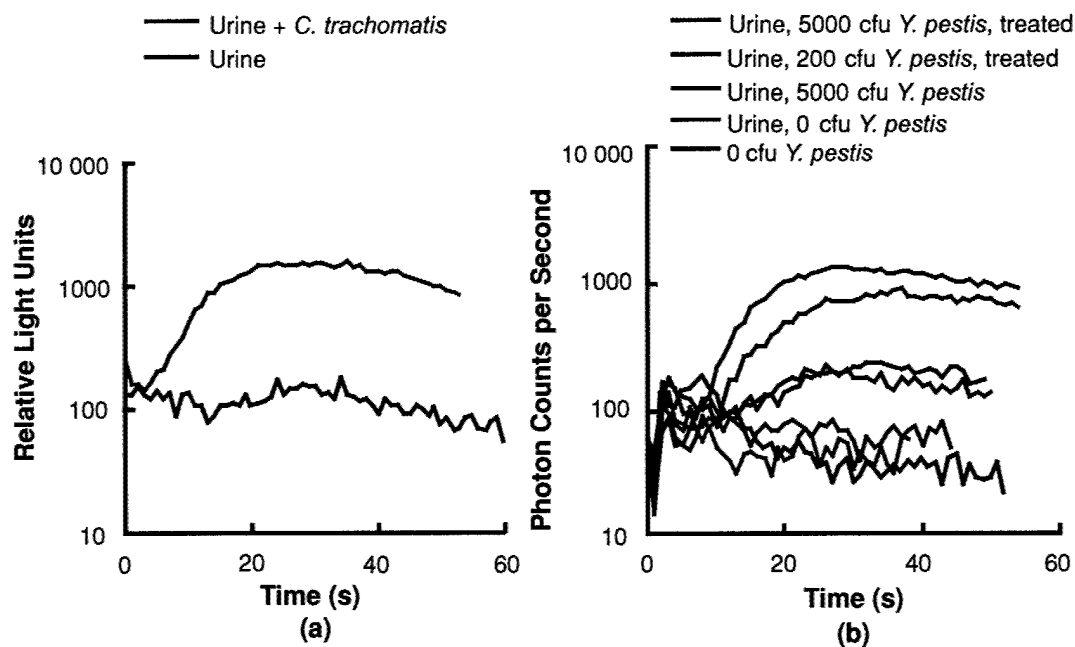


Figure 4-2. Results for urine prepared by filter-and-replace method after addition of (a) *C. trachomatis* and (b) *Y. pestis*. Because of the detection of as little as 200 cfu of *Y. pestis* in <5 min, this assay compares favorably with similar ones performed with nucleic acid tests, but is faster.

The detection of bacteria in human serum and whole blood with CANARY is demonstrated in Figure 4-3. Serum and plasma contain a nonspecific soluble activator that causes the CANARY cells to emit light with a different kinetic pattern than that from a specific interaction, as seen in Figure 4-3(a) (0 cfu of *Y. pestis* plus serum). This interferes with the ability of the assay to detect low numbers of pathogen (50 cfu of *Y. pestis* plus serum). However, if the serum is replaced with assay medium following centrifugation, the sensitivity is restored, as shown in Figure 4-3(b) (50 cfu of *Y. pestis* plus serum, replaced). Whole blood contains additional interferants that are released during the lysis of the red blood cells. When lysed whole blood (0.1 mL) is centrifuged and the supernatant replaced, the limit of detection (LOD) is reduced to 5000 cfu of *Y. pestis* (50,000 cfu/mL).

In an effort to increase the sensitivity of our assay with whole blood we have collaborated with M. Ewert of the University of South Florida, who is developing a preparation for whole blood utilizing enzyme treatment and centrifugation. Our results show that these treatments serve to decrease the interferants present in blood. In a single experiment, 50,000 cfu of *Y. pestis* was added to 6 mL of whole blood and processed according to Ewert's protocol. The processed samples were divided in half, each representing 25,000 cfu in 3 mL of whole blood (8333 cfu/mL), and gave a distinguishable signal when tested using the standard CANARY assay, as seen in Figure 4-3(c) (25,000 cfu per 3 mL of whole blood). Although there is still some loss of signal relative to the control (25,000 cfu), this result represents an improvement over the results described above. Additional preliminary experiments have indicated that modifications to this protocol should provide still further improvements in sensitivity.

Sputum contains a nonspecific activator, similar to what we have observed in human blood but distinct in that it is not removed by the filter-and-replace protocol, as shown in Figure 4-4(a) (0 cfu of *Y. pestis*). This interferant effectively reduces the LOD of the assay to 5000 cfu. However, preliminary experiments indicate that the protocol designed by Ewert will reduce the effects of the interferant in sputum by at least tenfold, shown by comparison of 0 cfu in Figure 4-4(a) with 0 cfu in Figure 4-4(b). Furthermore, when *Y. pestis* is added to the sample following preparation, there is no loss of signal relative to the control, demonstrating that there are no inhibitors present, as shown in Figure 4-4(b) by comparison of 100 cfu with 100 cfu, no sputum. Current efforts are focused on determining the LOD when *Y. pestis* is added to the sample prior to preparation.

M. S. Petrovick  
F. E. Nargi

## REFERENCE

1. T. H. Rider, M. S. Petrovick, F. E. Nargi, J. D. Harper, E. D. Schwoebel, R. H. Mathews, D. J. Blanchard, L. T. Bortolin, A. M. Young, J. Chen, and M. A. Hollis, *Science* **301**, 213 (2003).

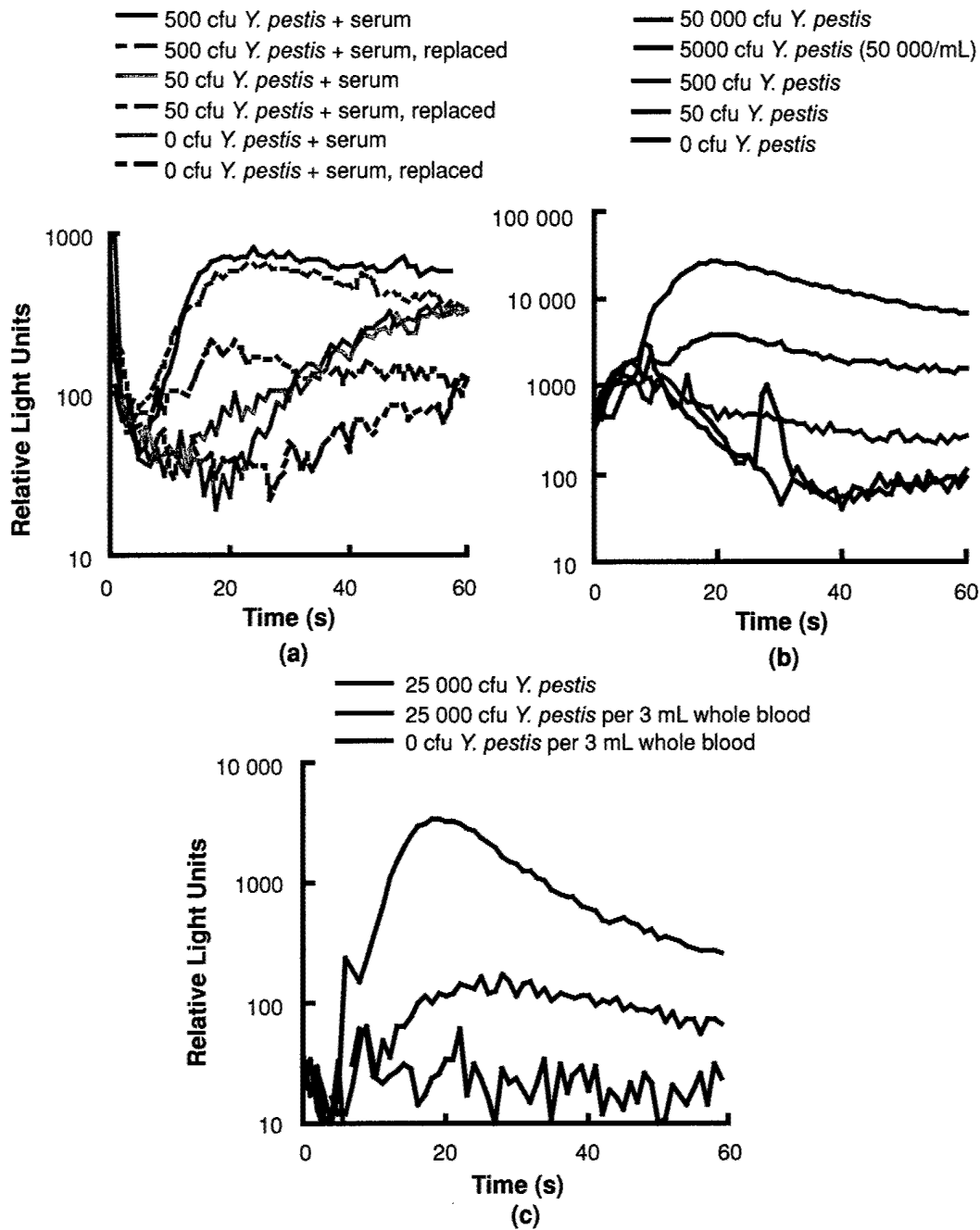


Figure 4-3. Detection of bacteria in human serum and whole blood with CANARY after (a) *Y. pestis* is added to 0.02 mL of serum, (b) *Y. pestis* is added to 0.1 mL of whole human blood, and (c) 50,000 cfu of *Y. pestis* is added to 6 mL of whole blood and processed according to M. Ewert's protocol. Although some loss of signal relative to the control (25,000 cfu) is still seen in (c), this result represents an improvement over (a) and (b).

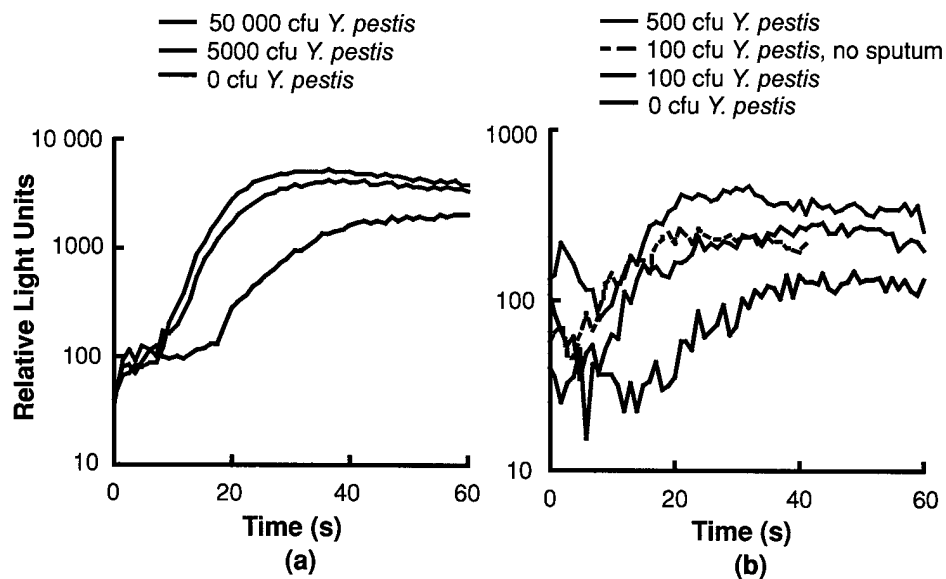


Figure 4-4. (a) Detection of bacteria added to sputum before processing by the filter-and-replace method, and (b) results using M. Ewert's protocol, which reduces the effects of the interferant by at least tenfold and allows the detection of 100 cfu of *Y. pestis* added to the processed sputum.

## 5. ADVANCED IMAGING TECHNOLOGY

### 5.1 INTENSITY-IMAGING FOCAL PLANE ARRAY USING GEIGER-MODE AVALANCHE PHOTODIODES

All-solid-state, all-digital photon-counting focal plane arrays (FPAs) have been developed that comprise Geiger-mode avalanche photodiodes (APDs) [1] integrated with a novel complementary metal-oxide semiconductor (CMOS) readout circuit. The circuit is based on the scalable architecture described earlier [2] and has been demonstrated to support 9-bit intensity imaging at 20,000 frames per second. It has a  $32 \times 32$  array of 1-bit pixels, each of which can latch and store one detection event during a short gate time (integration time). These 1-bit “microframes” are integrated on chip using a  $32 \times 32$  array of 9-bit counters. Transfer of detection counts from the pixel array to the counter array is done synchronously while all the APDs are being quenched and reset. A highly compact active quenching circuit in each pixel supports APD gate times as short as 10 ns and quench times under 40 ns.

Two variations of the CMOS circuit, designated T2 and T3, were designed and produced in two separate foundry submissions using a  $0.35\text{-}\mu\text{m}$  CMOS process. Figure 5-1(a) shows the T2 pixel circuit with 1-bit storage and active quenching circuitry. The T3 pixel circuit, shown in Figure 5-1(b), introduces two improvements over the T2 architecture. It electronically decouples the data store signal from the disarm signal, thereby reducing power dissipation by not disarming the APD at the end of every gate time. For large arrays, this can result in significant power savings. The T3 circuit also has a tunable reference voltage that can be used to set the trigger threshold of the active quenching circuit or to disable active quenching entirely. This capability facilitates testing to determine whether active quenching helps reduce

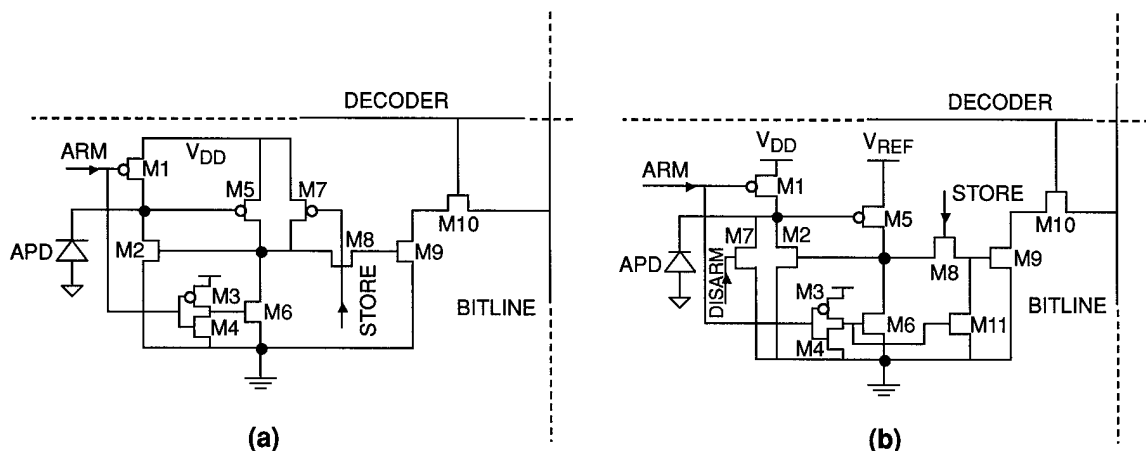


Figure 5-1. (a) 10-Transistor pixel with 1-bit storage and active quenching, used on the T2 readout integrated circuit (ROIC), and (b) 11-transistor pixel with 1-bit storage and active quenching, used on the T3 ROIC.

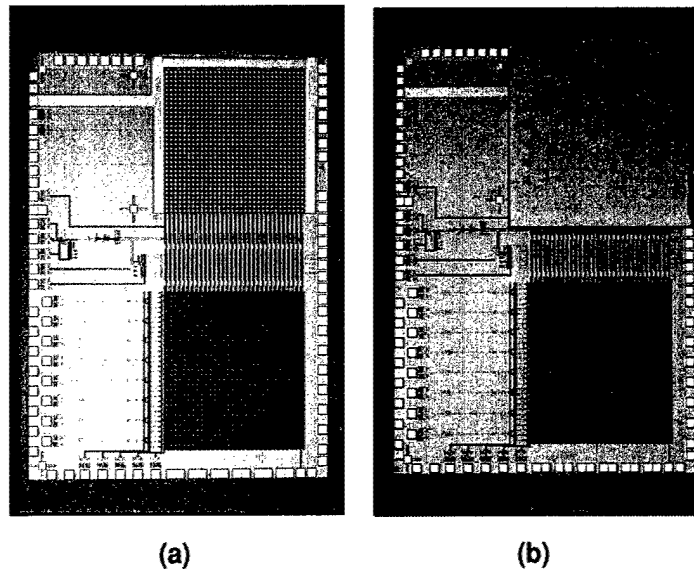
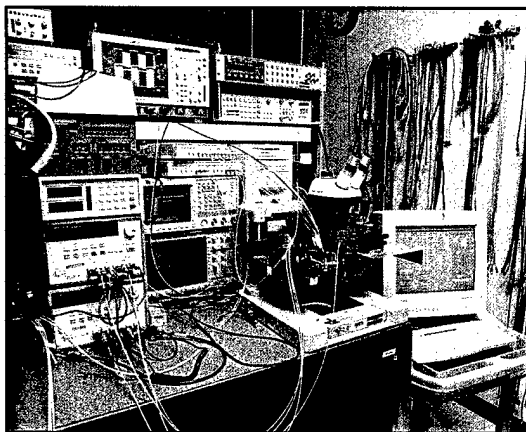


Figure 5-2. (a) Fully functional  $32 \times 32$   $50\text{-}\mu\text{m}$ -pixel pitch T2 ROIC using scalable complementary metal-oxide semiconductor (CMOS) readout circuit architecture, and (b) T2 ROIC based focal plane array (FPA) with bump-bonded  $16 \times 16$  array of  $100\text{-}\mu\text{m}$ -pixel pitch APDs.

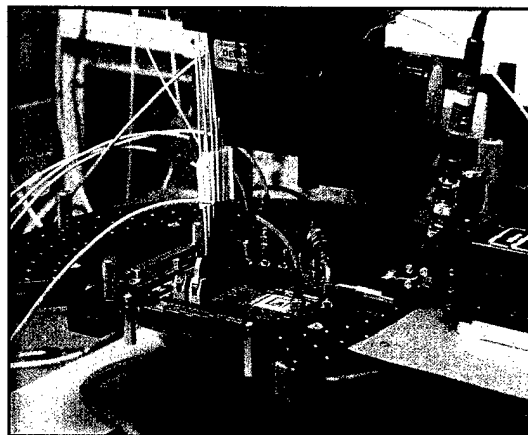
dark count rates, afterpulsing, and optical crosstalk. APDs have been bump bonded to the T3 chips, and the circuit has been tested and shown to function. Some preliminary measurements have been made on T2 and T3 FPAs, and the results appear to be encouraging.

We have successfully bump bonded  $16 \times 16$  arrays of  $100\text{-}\mu\text{m}$ -pixel and  $32 \times 32$  arrays of  $50\text{-}\mu\text{m}$ -pixel silicon APDs to T2 chips. Figure 5-2(a) shows a fully functional T2 chip, and Figure 5-2(b) shows a fully functional T2-based FPA with APDs that were thinned and glued to a quartz support wafer that was sawn and then bump bonded to the readout integrated circuit. Room-temperature test results for the first batch of T2-based focal planes were highly encouraging. APDs were operated successfully with 40-ns quench times and gate times as short as 10 ns. Measurements of the dark count rate at room temperature showed a strong dependence on APD overbias, quenching voltage, quench time, and gate time. Dark count rates in the range 20–930 kc/s were measured, depending on operating conditions. The dark count rates increased as quench times were reduced, but passive intensity imaging was still possible at the higher frame rates and shorter quench times. To verify correct operation as a passive photon-counting intensity imager, a 35-mm-focal-length Kreuznach C-Mount lens was suspended over the FPA and used to image a black cross. The benchtop test system used to collect the data is shown in Figure 5-3.

Two  $16 \times 16$  and one  $32 \times 32$  FPA, designated Alpha, Bravo, and Charlie, were tested. The  $16 \times 16$  image in Figure 5-4(a) was captured while operating Alpha with 250-ns gate time and  $1\text{-}\mu\text{s}$  quench time at



(a)

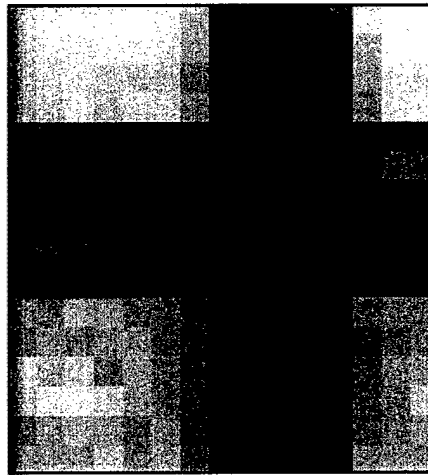


(b)

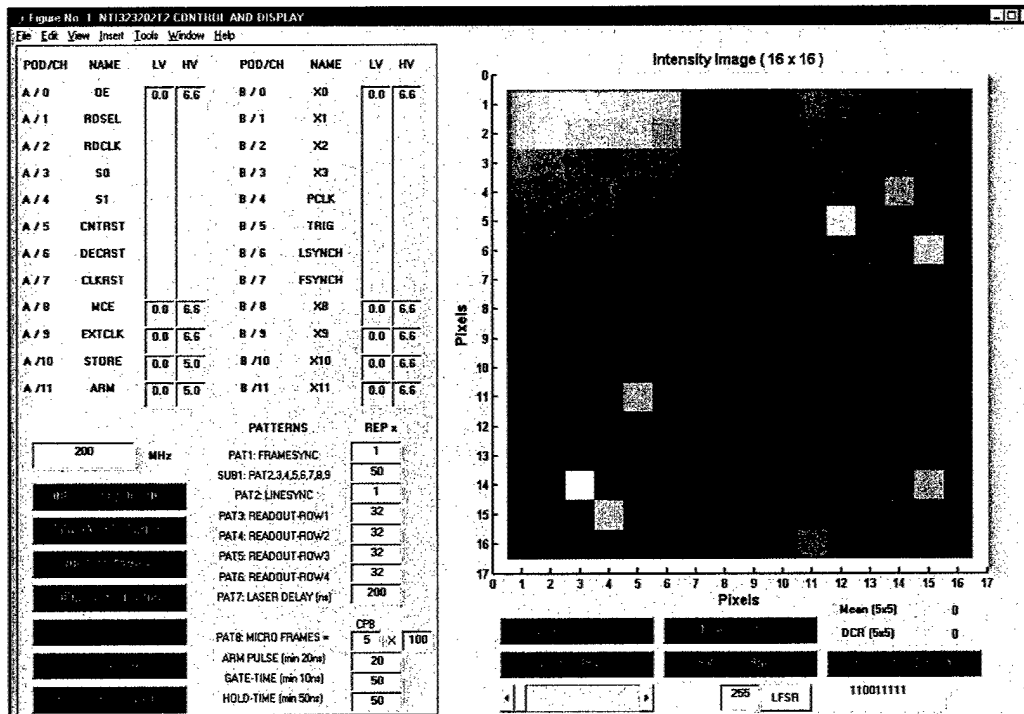
Figure 5-3. (a) Test equipment for measuring integrated CMOS readout circuits and FPAs, and (b) T2 ROIC based FPA undergoing testing.

1500 frames per second. The image in Figure 5-4(b), which shows the MATLAB graphical user interface window for camera control and display, was for operation of Bravo at  $>10,000$  frames per second with 50-ns gate time and 50-ns quench time. Figure 5-5 shows additional images of the cross obtained with various gate times and quench times. Correct imager operation was observed over a range of APD gate times from 10 ns to  $2\text{ }\mu\text{s}$  and quench times from 40 ns to  $2\text{ }\mu\text{s}$ .

Figures 5-6(a), 5-6(b), and 5-6(c) are plots of measured dark count rates as a function of APD overbias, quench time, and gate time, respectively. In Figure 5-6(b), the dark count rate for T2-Bravo increases by approximately 50%, as the APD quench time is reduced from  $1\text{ }\mu\text{s}$  to 40 ns. Improved anode connections that reduce the anode voltage ringing in T2-Charlie and T3-Alpha reveal dramatic improvement of the dark count rate over T2-Bravo. In Figure 6(c), the dark count rate increases as the gate time is shortened, indicating an elevated dark count rate in the early part of the gate-time interval. It is believed that a large fraction of these events are triggered by electronic ringing due to packaging parasitics associated with the anode connections to the APDs. FPAs with better packaging and extra bypass capacitors have led to much lower and more uniform dark count rates. Data from FPA Charlie with measures to reduce anode ringing show clear improvement over the earlier Bravo device. At 250-ns gate times, reducing the APD quench time from 1000 to 40 ns yields almost no increase in the dark count rate. At 50-ns gate time, T2-Charlie exhibits a dark count rate of 200,000, while at 1000-ns gate time the dark count rate is approximately 6 times less. T3-Alpha, by contrast, shows only a 3 to 1 increase in dark count rate for 50-ns gate time, while at longer gate times both T2 and T3 FPAs have nearly identical dark count rates as would be expected for bump-bonded APDs from the same wafer. What is most striking in the data is that T3-Alpha's dark count rate is 100,000 for 50-ns gate time and 40-ns quench time, while



(a)



(b)

Figure 5-4.  $16 \times 16$  Intensity images taken with two FPAs: (a) T2-Alpha, with 250-ns gate time, 1- $\mu$ s quench time, and ~1500 frames per second with 9-bit resolution, and (b) T2-Bravo, with 50-ns gate time, 50-ns quench time, and >10,000 frames per second with 9-bit resolution. The image in (b) shows the MATLAB graphical user interface window.



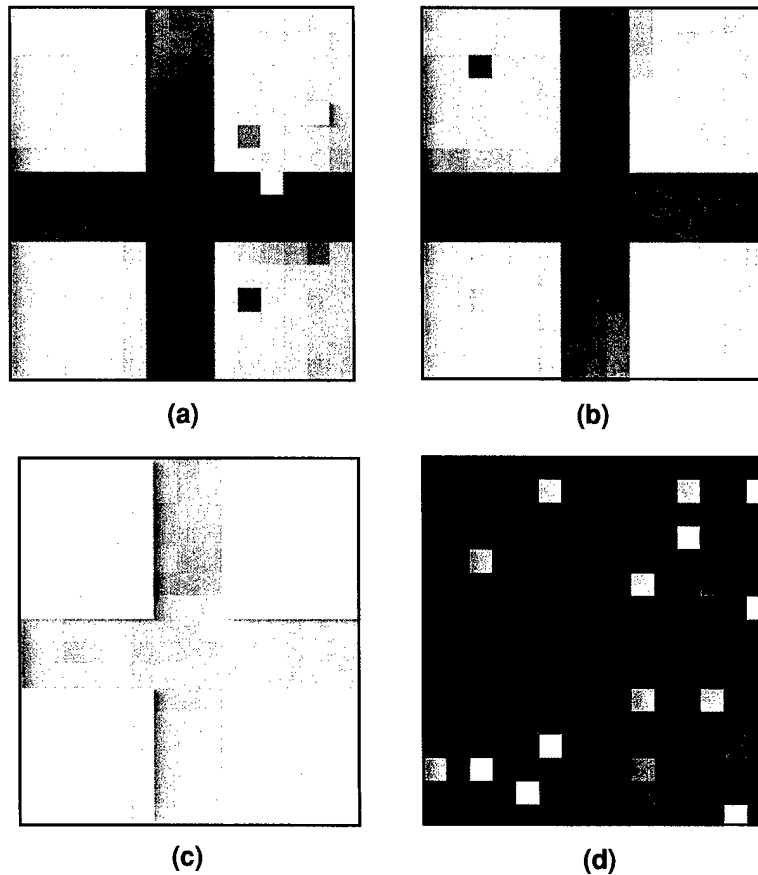


Figure 5-5.  $16 \times 16$  Intensity images taken with T2-Bravo with (a) 250-ns gate time, 1- $\mu$ s quench time, and  $\sim 1500$  frames per second with 9-bit resolution, (b) 250-ns gate time, 50-ns quench time, and  $\sim 5100$  frames per second with 9-bit resolution, (c) 1- $\mu$ s gate time, 50-ns quench time, and  $\sim 1900$  frames per second with 9-bit resolution, and (d) 10-ns gate time, 40-ns quench time, and  $\sim 14,000$  frames per second with 9-bit resolution.

T2-Charlie's is 200,000 for the same operating conditions. This difference is attributed to reduced anode ringing in the T3 ROIC when the APDs are rearmed, since the T3 pixel circuit only disarms an APD after it has fired, while T2 disarms the entire detector array after a gate-on interval. Therefore, when the array is rearmed less current is drawn in T3 than in T2, because only APDs that have fired are rearmed, leading to less ringing and a dramatically reduced dark count rate at shorter gate times.

The T2 and T3 chips support readout clock rates in excess of 200 MHz. All the images presented here were captured while reading data off chip using a 25-MHz readout clock, because the peripheral component interconnect (PCI) framegrabber used did not support higher clock rates. More advanced

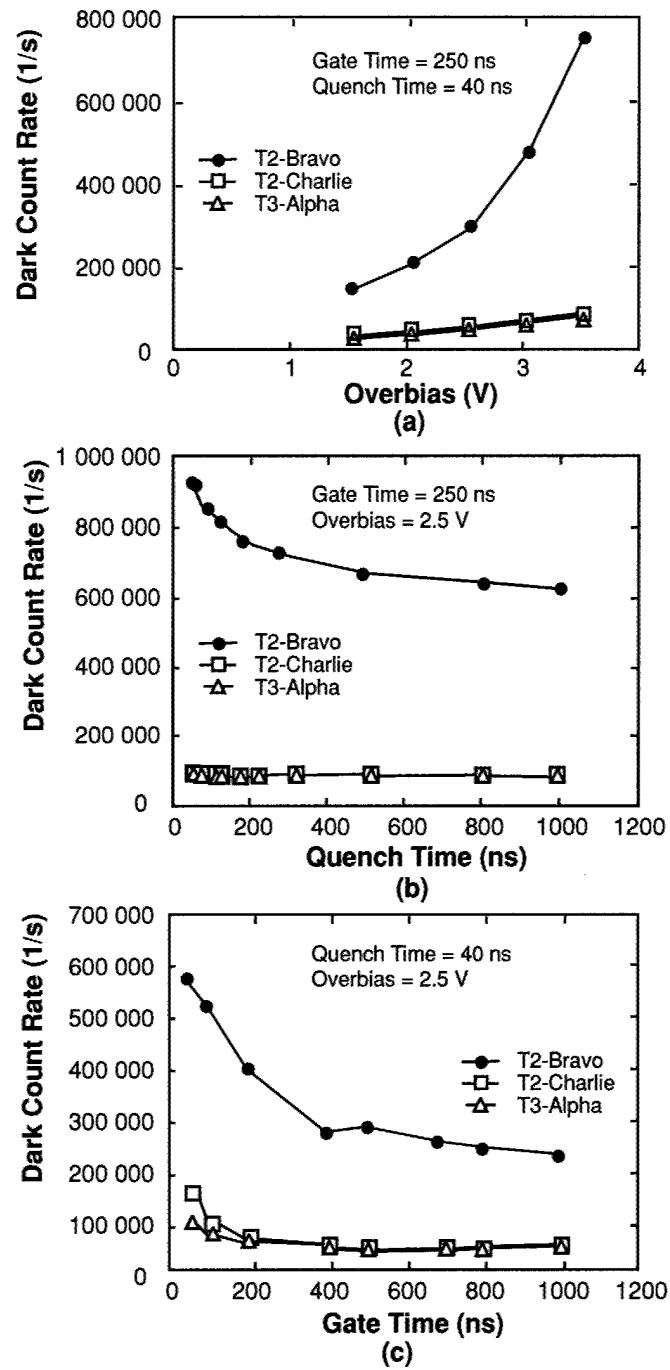


Figure 5-6. Avalanche photodiode (APD) dark count rate as a function of APD (a) overbias, (b) quench time, and (c) gate time.

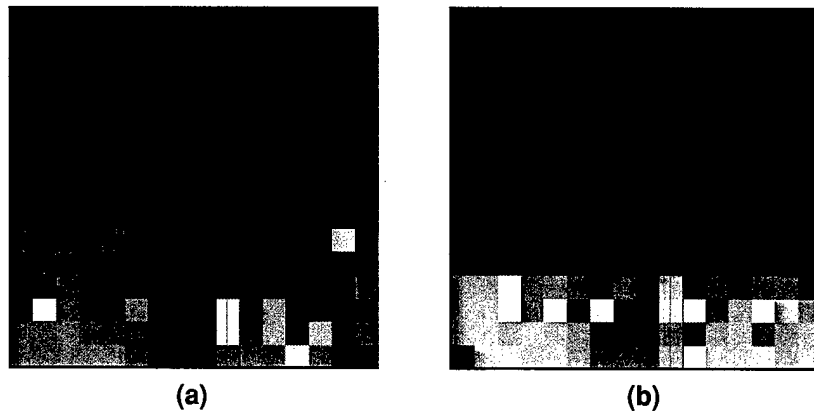


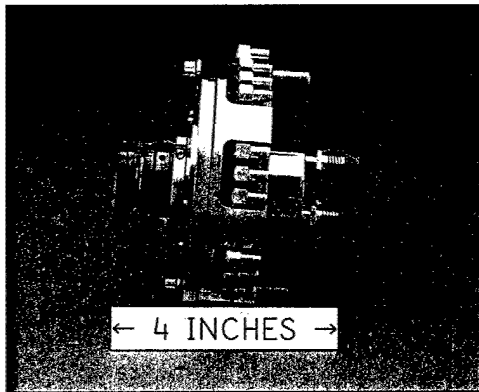
Figure 5-7.  $16 \times 16$  Intensity images taken with T2-Bravo with (a) 10-ns gate time and 20-ns quench time, and (b) 10-ns gate time and 10-ns quench time.

camera support electronics such as FIFO buffering will be implemented to support frame rates surpassing 30,000 frames per second.

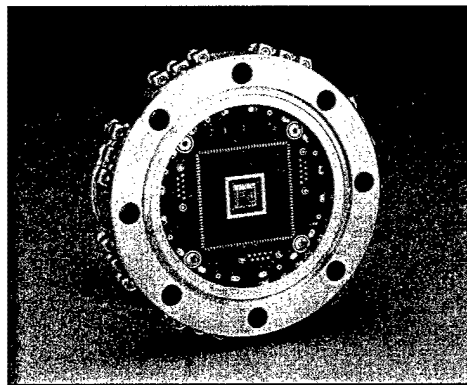
The time needed to transfer the 1-bit frame from the pixel circuit to the 9-bit counters gives an APD quench time of 40 ns for T2 and T3 readout circuits. Shorter quench times are possible by transferring only part of the frame. Figures 5-7(a) and 5-7(b) show images resulting from the integration of the bottom half and bottom quarter of the frame, respectively, corresponding to APD quench times of 20 and 10 ns. The set gate time was a short 10 ns for both images to prevent early firing in the gate interval from adding significantly to the APD quench time. Even at the short quench times, the image of the cross is observed, indicating the potential of the integrated APD photon detectors for high-speed intensity imaging.

A cryogenic camera system has been developed for photon-counting FPAs. The system was designed and built to facilitate testing of the silicon APD focal planes and to demonstrate APDs made with narrower-bandgap semiconductors for IR operation. The camera front end, shown in Figure 5-8, is designed to support FPAs operating over a temperature range from 80 K to room temperature. FPAs packaged with TE coolers can be mounted in the camera, or closed-cycle liquid nitrogen can be used to cool the device.

Although Figure 5-8(a) shows the hermetic camera package with a 35-mm-focal-length Kreuznach C-Mount lens, the unit will also accommodate custom optics. Its main component is a highly compact, tightly integrated printed circuit board (PCB), which accommodates a surface-mounted FPA package, along with support and interface electronics. A highly integrated module on the back of the PCB supports an IEEE 1394a Firewire interface for standardized high-speed transfer to a computer, eliminating the need for a framegrabber. The stainless steel PCB retainer has 24 hermetic coaxial connectors mounted to its



(a)



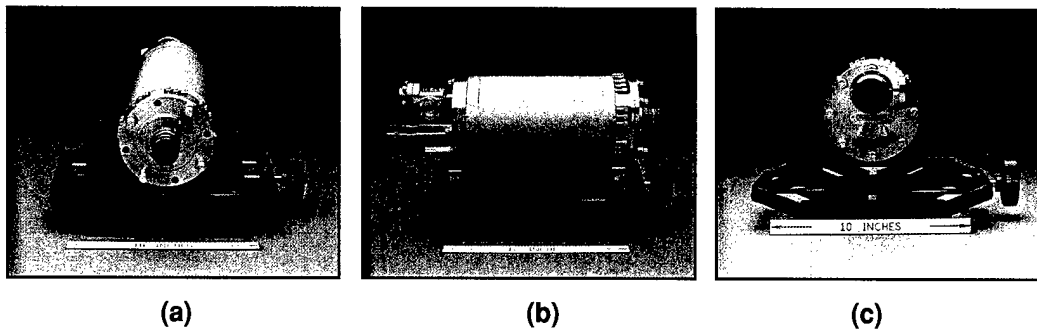
(b)

Figure 5-8. (a) Side view of all-stainless-steel front end of hermetically sealable cryogenic camera and (b) front view with hermetic window and imaging lens removed to reveal cooled FPA package and printed circuit board for support electronics.

exterior for general purpose input/output or power-feedthrough requirements. The glass-sealed center conductors from the 24 connectors enter the retainer wall radially and are soldered to exposed metal contact pads on the back side of the PCB. Four holes on the periphery of the PCB, shown in Figure 5-8(b), allow tight fastening of the PCB/FPA/heatsink assembly to metal supports (not visible) that are milled into the interior of the PCB retainer. A channeled heatsink partially visible in Figure 5-8(a) is fixed to the PCB and makes thermal contact with the back of the FPA package for heat extraction. Threaded, metal-gasket sealed connectors with affixed protective covers can be used to attach flexible metal bellows for closed-cycle refrigerant circulation. The camera front end in a hermetic housing is shown in Figure 5-9.

The imaging devices reported here are, to the best of our knowledge, the first FPAs that perform photon-counting intensity imaging using Geiger-mode APD arrays integrated with CMOS digital counting circuits. The camera system described will be used to investigate the reduction of dark count rate and quantify imager performance metrics such as pixel-to-pixel crosstalk, detection efficiency, and intrapixel response. We will also develop a photon transfer curve test routine to evaluate FPA noise. Miniaturization of the camera system will be pursued along with scaling up the format of the focal plane and demonstration of focal planes at longer wavelengths using compound semiconductor APDs.

A. G. Stern	B. F. Aull
B. B. Kosicki	R. K. Reich
B. J. Felton	A. H. Loomis
D. J. Young	D. Rathman
R. Slattery	J. Aversa
K. Percival	R. B. Holloway
C. D. Jones	



*Figure 5-9. Camera dewar: (a) front view, (b) side view showing refrigerant feedthroughs left beneath atmosphere control valve, and (c) back view showing atmosphere control valve, coolant, and electrical feeds.*

#### REFERENCES

1. B. F. Aull, A. H. Loomis, D. J. Young, R. M. Heinrichs, B. J. Felton, P. J. Daniels, and D. J. Landers, *Lincoln Lab. J.* **13**, 335 (2002).
2. Solid State Research Report, Lincoln Laboratory, MIT, 2001:4, p. 25.

## 6. ANALOG DEVICE TECHNOLOGY

### 6.1 TEMPERATURE DEPENDENCE OF INTERMODULATION DISTORTION IN YBCO

Nonlinear effects are one of the limits of performance of high- $T_c$  materials in microwave-frequency devices. Intermodulation distortion (IMD) is a deleterious effect observed in all superconducting materials, especially in high- $T_c$  superconductors (HTS). In practical devices such as filters, the IMD degrades performance, even at relatively low power. Understanding of its origins, however, is lacking.

It is well known that in the HTS materials intrinsic nonlinearities are present. Dahm and Scalapino [1],[2] predicted that the nonlinearities would lead to IMD. They found that the IMD would increase at low temperatures because of the nonlinear Meissner effect [3]. Until now, these effects have not been observed experimentally. Here, we demonstrate the upturn of IMD at low temperature in the best-quality films. Those with more fabrication defects do not show evidence for the intrinsic behavior.

The IMD measurements reported here have been carried out with six YBCO films from various sources. Only the results from the best film are summarized. For a more complete account, see [4]. The films were patterned and assembled with ground planes to form stripline resonators [5]. The third-order IMD was measured by applying two closely spaced tones of equal power at frequencies  $f_1$  and  $f_2$  to the resonator. The third-order mixing products at frequencies  $2f_1 - f_2$  and  $2f_2 - f_1$  are then measured in a spectrum analyzer as a function of the input power.

Figure 6-1 shows the measurements of the IMD, normalized for  $Q$  and insertion loss [4], as a function of the circulating power in the resonator for a pulsed-laser-deposited (PLD) pure  $\text{YBa}_2\text{Cu}_3\text{O}_{7-\delta}$ .

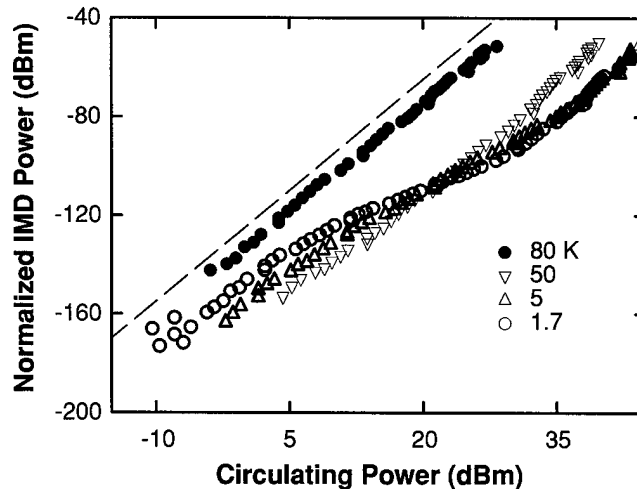


Figure 6-1. Intermodulation distortion (IMD) vs circulating power for selected temperatures. This is for a pulsed-laser deposited film of  $\text{YBa}_2\text{Cu}_3\text{O}_{7-\delta}$ . The dashed line illustrates slope 3, an indication of a  $P_{\text{circ}}^3$  dependence.

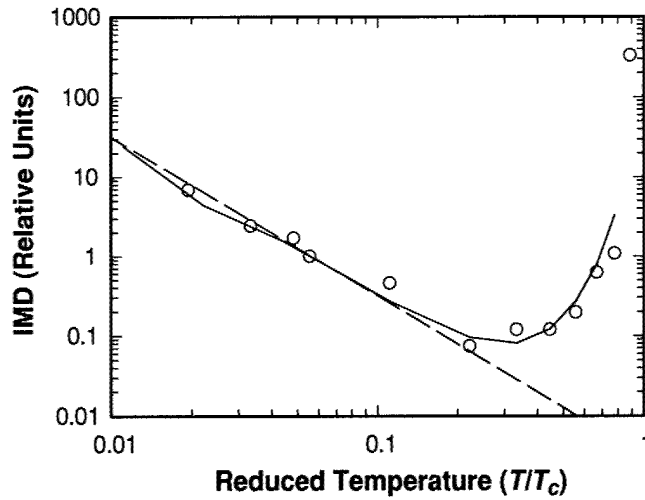


Figure 6-2. Comparison of data and theory. The open circles are the IMD data, the solid line is the calculation of  $d$ -wave theory, and the dashed line shows  $1/T^2$  behavior.

film for several temperatures. At low powers, the slope is 3, but at intermediate power the slope changes over to less than 2 for the lowest temperatures, and subsequently, at the highest powers the slope becomes 3 once again. Note that at the lowest powers the IMD increases as the temperature decreases. This is counter to the normal expectation that superconductivity improves as the temperature is lowered.

The open circles in Figure 6-2 show the temperature dependence of the IMD in this same film as a function of temperature at a circulating power of 5 dBm. This is compared with a theoretical calculation discussed below.

A microscopic calculation of the momentum-space constitutive relation (CR), which relates the current density and vector potential, was carried out. For type II superconductors, the CR linear approximation and Maxwell's equations yield the London equations. Here, the linear CR is extended to include the third-order term. This extended CR yields the intermodulation power from the nonlinear penetration depth. The calculated intermodulation-power slope and the low-temperature penetration depth variation compare well with our data. Figure 6-2 shows the comparison of the measured IMD and the calculation in relative units. As can be seen, the agreement is quite good; both experiment and calculation show a  $1/T^2$  divergence at low temperatures.

The IMD calculation yields two distinct power-level regimes that correspond to two of the power-level regimes shown in Figure 6-1. In the low-power regime, the calculated current-dependence of the penetration depth is quadratic, yielding a slope of 3 in the plot of IMD vs circulating power. In the medium-power regime, the CR current-dependence becomes nonanalytic [1]–[3], in the form of a

fractional power of the absolute value of the current. The corresponding IMD-power slope compares well with the data in the intermediate power region of Figure 6-1.

The microscopic calculation is based on solving the Gorkov equation to third order under some controlled approximations. The ensuing CR implies that the nonlinear current component is also nonlocal in space, extending over a penetration depth, implying that the nonlinear penetration depth is approximately uniform in space. Consequently, the penetration depth is extracted from the CR long-wavelength limit, as in the London theory. The theoretical calculations will be presented in detail in a future publication [6].

We have observed the nonlinear Meissner effect in YBCO thin films by measurements of the IMD as a function of temperature extended to low temperatures. This is an indication that we are observing intrinsic nonlinearities. The films show evidence of extrinsic effects as well. For the best film, comparisons with theory yield good agreement with the IMD temperature and power dependence. Other films show a low-temperature increase, but significant departures from the theory result from extrinsic contributions to the IMD.

D. E. Oates	S.-H. Park
D. Agassi*	G. Koren*

#### REFERENCES

1. T. Dahm and D. J. Scalapino, *Phys. Rev. B* **60**, 13125 (1999).
2. T. Dahm and D. J. Scalapino, *J. Appl. Phys.* **81**, 2002 (1997).
3. S. K. Yip and J. A. Sauls, *Phys. Rev. Lett.* **69**, 2264 (1992).
4. D. E. Oates, S.-H. Park, D. Agassi, and G. Koren, to be published in *Proceedings of the European Conference on Applied Superconductivity (EUCAS) 2003* (Institute of Physics Publishing, Bristol, UK).
5. D. E. Oates, A. C. Anderson, and P. M. Mankiewich, *J. Superconduct.* **3**, 2519 (1990).
6. D. Agassi and D. E. Oates, unpublished material.

---

\*Author not at Lincoln Laboratory.



## 7. ADVANCED SILICON TECHNOLOGY

### 7.1 ELIMINATION OF PARASITIC CHANNELS IN FULLY DEPLETED SOI CMOS

In order to realize sharper device turn-on characteristics in our 180-nm fully depleted silicon-on-insulator (FDSOI) technology [1], we have carefully studied subthreshold behavior of both  $n$ MOS and  $p$ MOS devices. A shoulder in the subthreshold characteristic can result from a secondary channel in parallel with a primary one, much narrower and with lower threshold. We have observed two types of subthreshold shoulders: local gate penetration by implanted boron (a new effect) and parasitic edge conduction (a well-known effect [2]). Although a 6-keV B implant has an expected range less than 1/10 of the 200-nm-thick poly gate used in our process, we show that local gate penetration can occur. We have successfully modified our FDSOI process to eliminate the impact of both effects, substantially improving device performance and circuit yield.

The first mechanism, local gate dopant penetration, affected a significant fraction of standard 0.18- $\mu$ m gate length  $p$ MOS devices, shown in Figure 7-1, across a 150-mm-diameter wafer. However, the same effect was not seen with longer 0.50- $\mu$ m devices, as shown by the subthreshold current-voltage (I-V) plots in Figure 7-2. As seen in Figures 7-1 and 7-3, shoulders were found to be present in standard devices, in which a channel edge is coincident with a SOI island edge, as well as in H-gate edgeless devices, in which the channel does not include a SOI island edge.

To determine the origin of the large  $p$ MOS shoulders, we fabricated a series of devices with a variety of gate dielectrics (4- and 7-nm thermal oxide, and 4-nm nitrous oxide; see Table 7-1). In all cases, with a  $p$ MOS  $p^+$  source-drain implant of 6- or 10-keV B, large shoulders were present. Similar occurrence of

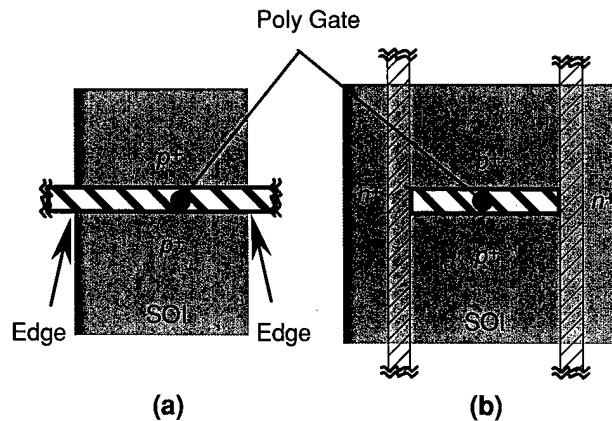


Figure 7-1. Schematic (top view) of (a) standard (edge) and (b) H-gate (edgeless)  $p$ MOS devices.

shoulders for both 4- and 7-nm gate oxides suggested that local B diffusion through the gate oxide was not the culprit. To determine if lateral B diffusion from the source-drain extension into the channel caused *p*MOS shoulders, we fabricated devices with spacer widths of 75 and 150 nm, no extension implant, and a 6-keV B source-drain implant. Again, *p*MOS shoulders were observed for both spacer widths.

We then fabricated a series of devices with different gate stacks (undoped poly, in-situ doped poly, in-situ doped poly with implant mask) and varied the energy and species used for the  $p^+$  implant (6-keV B, 2.5-keV B, and 20-keV  $\text{BF}_2$ ), as summarized in Table 7-1. The results clearly showed, for the 6-keV B  $p^+$  implant, *p*MOS devices had large shoulders for both undoped and in-situ doped poly Si gates. A noteworthy observation was that *p*MOS shoulders affected all 100- $\mu\text{m}$ -wide devices but almost no 0.6- $\mu\text{m}$ -wide devices, as seen in Figure 7-4, suggesting a randomly distributed phenomenon. By comparison, with 20-keV  $\text{BF}_2$  or 2.5-keV B, no *p*MOS shoulders were observed, as shown in Figures 7-5 and 7-6. Also, for in-situ doped gates with an implant mask protecting the gate from the  $p^+$  implant, no shoulders were observed. We measured *p*MOS gate doping and found a reduction of ~30% for the 2.5-keV implant in comparison to the 6-keV B implant. Suppression of *p*MOS shoulders was clearly evident in comparing summary  $I_{\text{on}}$  vs  $I_{\text{off}}$  vs gate length plots for 21 devices across a 150-mm-diameter wafer, as shown in Figures 7-7 and 7-8, with 6- and 2.5-keV B implants, respectively.

From these results, we concluded that large *p*MOS shoulders were not the result of lateral B diffusion, but rather local gate penetration of  $p^+$  implant atoms into the channel region, creating isolated parasitic channels with lower threshold. We examined poly gates by scanning electron microscopy, with results shown in Figure 7-9, and by atomic force microscopy, and discovered poly nodules whose density

**TABLE 7-1**  
**Summary of Parameters Used to Identify the Cause of *p*MOS Shoulders\***

Parameter	Variations
Gate dielectric	4- and 7-nm thermal oxide 4-nm nitrous oxide
Gate	Undoped poly In-situ doped poly In-situ doped poly with oxide implant mask
$p^+$ Implant	2.5-, 6-, and 10-keV B 20-keV $\text{BF}_2$
*All <i>p</i> MOS devices had shoulders except those with a 2.5-keV B or 20-keV $\text{BF}_2$ implant, or an in-situ doped gate with an oxide implant mask.	

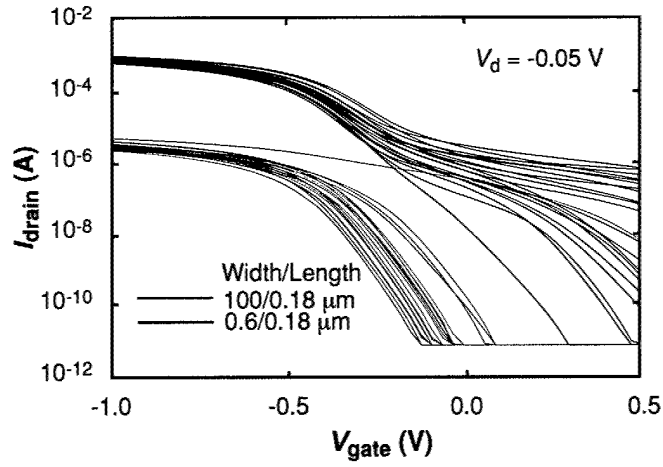


Figure 7-4. Subthreshold I-V curves for standard pMOS with 6-keV B  $p^+$  implant, 21 devices each, across a 150-mm-diameter wafer.

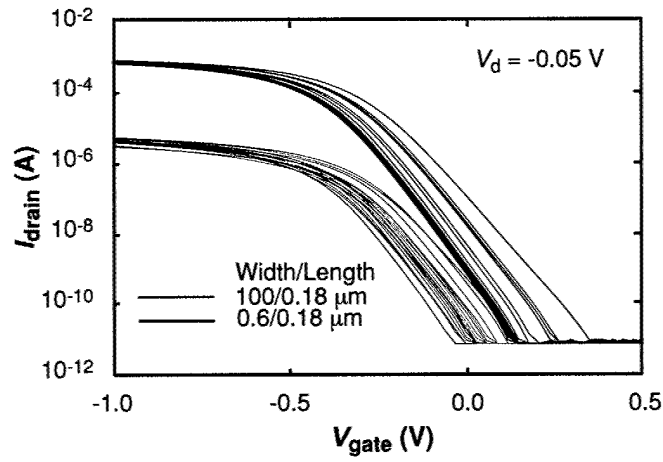


Figure 7-5. Subthreshold I-V curves for standard pMOS with 20-keV  $\text{BF}_2$   $p^+$  implant, 21 devices each, across a 150-mm-diameter wafer.

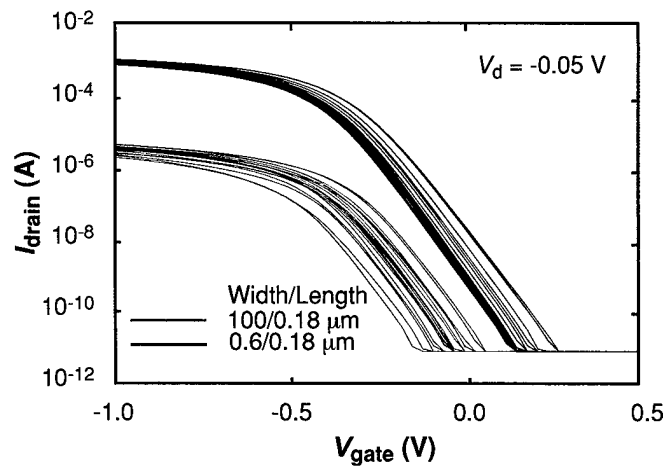


Figure 7-6. Subthreshold  $I$ - $V$  curves for standard  $p$ MOS with 2.5-keV  $B$   $p^+$  implant, 21 devices each, across a 150-mm-diameter wafer.

was similar to the occurrence of the  $p$ MOS shoulders. Although an exact mechanism resulting in the large  $p$ MOS shoulders is not clear, one possibility is  $B$  ion channeling associated with the poly nodule, causing local penetration into the channel region.

The second mechanism, parasitic edge conduction, was characterized by comparing subthreshold  $I_d$  vs  $V_g$  for standard edge and H-gate edgeless  $n$ MOS devices, as shown in Figure 7-10. To suppress edge-related shoulders, edge channel threshold was increased by reducing buried oxide (BOX) loss to minimize gate wraparound, and by adding an edge implant to locally increase channel doping. By implementing these process modifications, we have successfully suppressed shoulders associated with edge conduction, as seen in Figure 7-11.

In summary, we have identified and corrected two different mechanisms giving rise to low-threshold parasitic channels and subthreshold shoulders in our FDSOI process. The  $p$ MOS shoulders resulting from local gate penetration were eliminated by utilizing a  $p^+$  implant with reduced implant range, and edge shoulders were eliminated by incorporating an edge implant and reducing BOX loss. These process modifications have significantly improved subthreshold behavior of both  $n$ MOS and  $p$ MOS devices and have substantially improved performance and yield of complex circuits.

C. K. Chen	C. L. Chen
P. W. Wyatt	P. Gouker
J. A. Burns	D. R. W. Yost
M. Fritze	V. Suntharalingam
C. L. Keast	

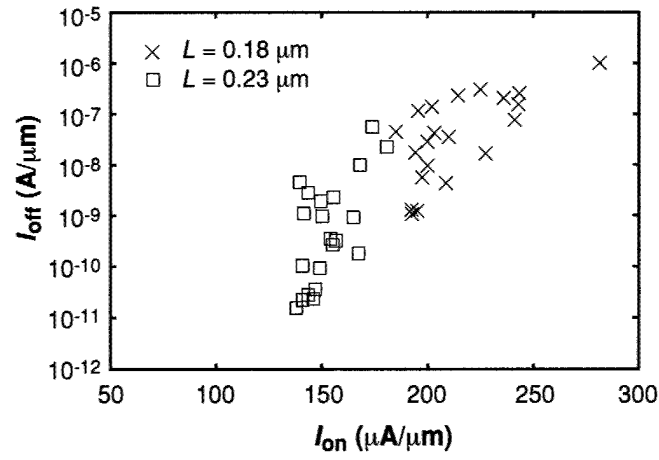


Figure 7-7.  $I_{on}$  vs  $I_{off}$  vs gate length for standard pMOS with 6-keV B  $p^+$  implant.  $V_d = -1.5$  V;  $I_{on}$  at  $V_g = -1.5$  V;  $I_{off}$  at  $V_g = 0.0$  V.

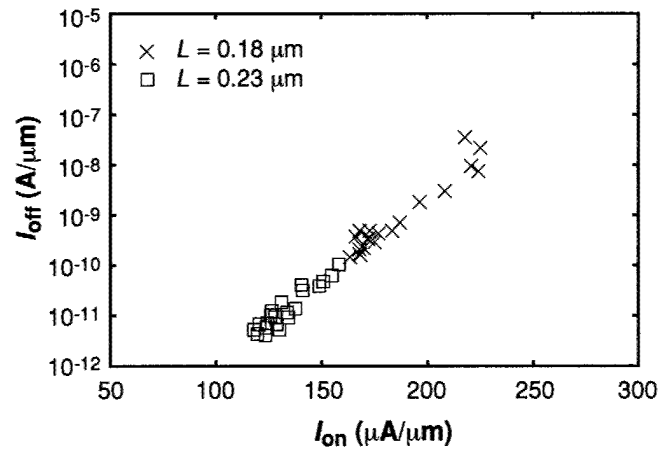


Figure 7-8.  $I_{on}$  vs  $I_{off}$  vs gate length for standard pMOS with 2.5-keV B  $p^+$  implant.  $V_d = -1.5$  V;  $I_{on}$  at  $V_g = -1.5$  V;  $I_{off}$  at  $V_g = 0.0$  V.

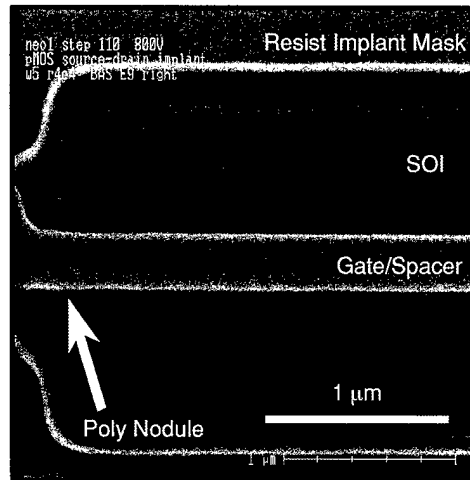


Figure 7-9. Plan view scanning electron micrograph of a standard 100/0.18- $\mu\text{m}$  device, showing the presence of a poly nodule.

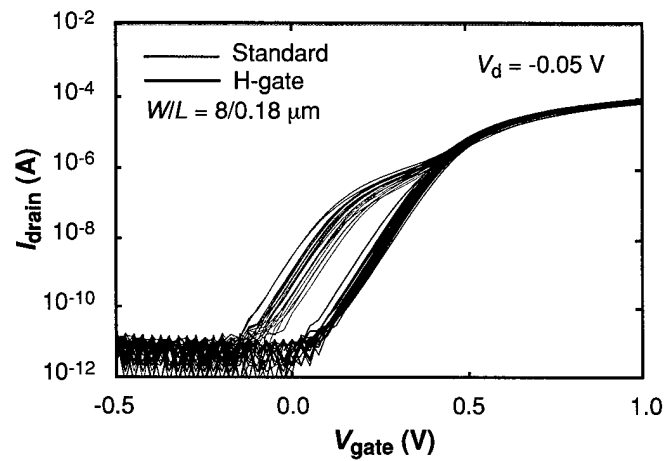


Figure 7-10. Edge vs edgeless nMOS subthreshold I-V curves, without edge implant, 21 devices each, across a 150-mm-diameter wafer.

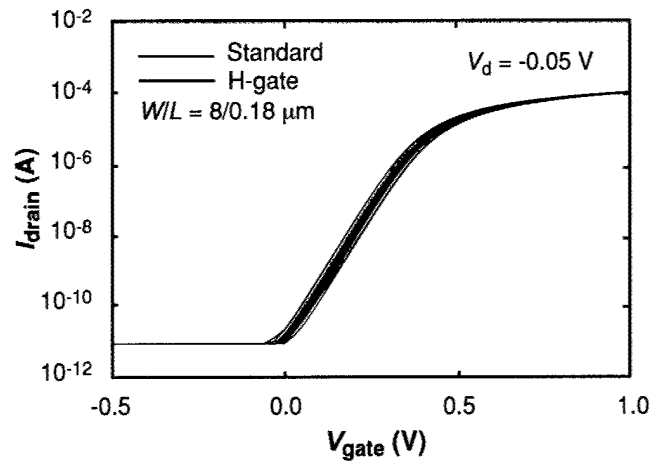


Figure 7-11. Edge vs edgeless nMOS subthreshold I-V curves, with edge implant, 21 devices each, across a 150-mm-diameter wafer.

#### REFERENCES

1. C. L. Chen, R. H. Mathews, J. A. Burns, P. W. Wyatt, D-R. Yost, C. K. Chen, M. Fritze, J. M. Knecht, V. Suntharalingam, A. M. Soares, and C. L. Keast, *IEEE Electron Device Lett.* **21**, 497 (2000).
2. T. Iizuka, K. Chiu, and J. L. Mell, *International Electron Devices Meeting Technical Digest* (IEEE, New York, 1981), p. 380.

REPORT DOCUMENTATION PAGE				Form Approved OMB No. 0704-0188	
The public reporting burden for this collection of information is estimated to average 1 hour per response, including the time for reviewing instructions, searching existing data sources, gathering and maintaining the data needed, and completing and reviewing the collection of information. Send comments regarding this burden estimate or any other aspect of this collection of information, including suggestions for reducing the burden, to Department of Defense, Washington Headquarters Services, Directorate for Information Operations and Reports (0704-0188), 1215 Jefferson Davis Highway, Suite 1204, Arlington, VA 22202-4302. Respondents should be aware that notwithstanding any other provision of law, no person shall be subject to any penalty for failing to comply with a collection of information if it does not display a currently valid OMB control number.					
PLEASE DO NOT RETURN YOUR FORM TO THE ABOVE ADDRESS.					
1. REPORT DATE (DD-MM-YYYY) 15-11-2003		2. REPORT TYPE Quarterly Technical Report		3. DATES COVERED (From - To) 1 August - 31 October 2003	
4. TITLE AND SUBTITLE  Solid State Research				5a. CONTRACT NUMBER F19628-00-C-0002	
				5b. GRANT NUMBER	
				5c. PROGRAM ELEMENT NUMBER	
6. AUTHOR(S)  David C. Shaver				5d. PROJECT NUMBER 221	
				5e. TASK NUMBER 961	
				5f. WORK UNIT NUMBER	
7. PERFORMING ORGANIZATION NAME(S) AND ADDRESS(ES) Lincoln Laboratory, MIT 244 Wood Street Lexington, MA 02420-9108				8. PERFORMING ORGANIZATION REPORT NUMBER 2003:4	
9. SPONSORING/MONITORING AGENCY NAME(S) AND ADDRESS(ES) HQ Air Force Materiel Command AFMC/STSC Wright-Patterson AFB, OH 45433-5001				10. SPONSOR/MONITOR'S ACRONYM(S)	
				11. SPONSOR/MONITOR'S REPORT NUMBER(S) ESC-TR-2003-083	
12. DISTRIBUTION/AVAILABILITY STATEMENT Approved for public release; distribution is unlimited.					
13. SUPPLEMENTARY NOTES None					
14. ABSTRACT  This report covers in detail the research work of the Solid State Division at Lincoln Laboratory for the period 1 August through 31 October 2003. The topics covered are Quantum Electronics, Electro-optical Materials and Devices, Submicrometer Technology, Biosensor and Molecular Technologies, Advanced Imaging Technology, Analog Device Technology, and Advanced Silicon Technology. Funding is provided by several DoD organizations—including the Air Force, Army, DARPA, MDA, Navy, NSA, and OSD—and also by the DOE, NASA, and NIST.					
15. SUBJECT TERMS quantum electronics    submicrometer technology    advanced imaging technology    A/D converters    YBCO films electro-optical devices    biosensor technology    analog device technology    aerosol sensing    metal oxide semiconductors materials research    molecular technology    microchip lasers    focal plane arrays    SOI technology					
16. SECURITY CLASSIFICATION OF:			17. LIMITATION OF ABSTRACT	18. NUMBER OF PAGES	19a. NAME OF RESPONSIBLE PERSON
a. REPORT	b. ABSTRACT	c. THIS PAGE			19b. TELEPHONE NUMBER (Include area code)
Unclassified	Unclassified	Unclassified	None	68	